LARGE EDDY SIMULATION OF TURBULENT FLOWS USING THE LATTICE BOLTZMANN METHOD

A Thesis Submitted to the College of

Graduate and Postdoctoral Studies

In Partial Fulfillment of the Requirements

For the Degree of Master of Science

In the Department of Mechanical Engineering

University of Saskatchewan

Saskatoon

By

MING TENG

PERMISSION TO USE

In presenting this thesis in partial fulfillment of the requirements for a Postgraduate degree from the University of Saskatchewan, I agree that the Libraries of this University may make it freely available for inspection. I further agree that permission for copying of this thesis/dissertation in any manner, in whole or in part, for scholarly purposes may be granted by the professor or professors who supervised my thesis/dissertation work or, in their absence, by the Head of the Department or the Dean of the College in which my thesis work was done. It is understood that any copying or publication or use of this thesis/dissertation or parts thereof for financial gain shall not be allowed without my written permission. It is also understood that due recognition shall be given to me and to the University of Saskatchewan in any scholarly use which may be made of any material in my thesis.

Requests for permission to copy or to make other uses of materials in this thesis in whole or part should be addressed to:

Head of the Department of Mechanical Engineering

57 Campus Drive

University of Saskatchewan

Saskatoon, Saskatchewan S7N 5A9

Canada

OR

Dean

College of Graduate and Postdoctoral Studies

University of Saskatchewan

116 Thorvaldson Building, 110 Science Place

Saskatoon, Saskatchewan S7N 5C9

Canada

ABSTRACT

Turbulent flow is a complex fluid phenomenon because of its disordered and chaotic flow patterns. Analysis of such flows presents practical significance and is widely performed using either experiments or simulations. The numerical simulation, or computational fluid dynamics (CFD) is one powerful technique; traditionally, it is based on the Navier-Stokes equations. A novel numerical approach called the lattice Boltzmann method (LBM) has developed quickly over the past decades, and this method is based on an entirely different mechanism. The current thesis seeks to present an investigation of turbulent flows that was performed using the LBM.

Considered to be a potential alternative to the traditional Navier-Stokes equations, LBM essentially demonstrates two unique advantages, namely being simple in algorithm and suitable for parallelization. These two features arise from the fact that there is no pressure solver required to correct the velocity field, and that LBM follows a streaming-collision procedure. The current research used a multiple relaxation time (MRT) collision model to study three-dimensional turbulent flows based on a D3Q19 lattice model. Four types of boundary schemes were introduced in the current study: halfway bounce-back no-slip boundary condition, periodic boundary condition, precursor inflow boundary condition and constant pressure boundary condition. The driving mechanism of the fluid flow in the current LBM scheme was realized via a source term in the particle distribution functions. A three-dimensional sinusoidal perturbation was used in the initial condition to efficiently trigger turbulence in the developing stage of the flow simulation.

Inherent uniformity of the LBM imposes a constraint over its practical applications to complex flows. The current study attempted to solve this issue by studying a volumetrically formulated local grid refinement. This scheme was selected since it preserves the laws of conservation, and in addition, implementation of the scheme is fairly straightforward. Due to the time constraint, this thesis only considered a laminar channel flow for a Reynolds number of $Re \approx 1.08$ as a preliminary test case. The regions near the walls were refined locally using this scheme. The scheme achieves satisfactory agreement of the velocity profile with the analytical solution.

A simulation of turbulent channel flow for a Reynolds number of $Re_\tau \approx 230$ was implemented to validate the performance of the developed code. The mean velocity profiles and Reynolds stress profiles were determined based on averaging 174,000 time steps after reaching quasi-steady state. These results were compared to those from the literature for a Reynolds number of $Re_\tau \approx 180$. The results are in good agreement, although some small over-predictions are observed due to the difference in Reynolds numbers. Instantaneous vorticity visualization in transverse cross-sections revealed the dominance of small-scale wall-induced vortices in the near wall regions. These structures tend to expand in size with increasing distance away from the wall. Instantaneous vortex structures were visualized using the second invariant criterion. Typical hairpin structures were not clearly evident, although elongated streaks were clearly captured in the near wall regions.

As an example of a more complex flow, a large eddy simulation (LES) of turbulent flow over two cubic prisms was realized for a Reynolds number of $Re_H \approx 3350$, based on the bulk velocity and prism height, H. A pre-cursor inflow was used to provide the information for the inlet boundary condition and a constant pressure was specified at the outlet of solution domain. The LES LBM used the standard Smagorinsky subgrid-scale (SGS) model with wall-damping. Analysis of the flow features was implemented from three perspectives: mean flow patterns, instantaneous flow features and energetic structures using a Proper Orthogonal Decomposition (POD). A symmetric mean flow pattern was evident in a horizontal plane located at the mid-height of the cubes. Recirculation regions were well observed, and the locations were found to be reasonably consistent with those identified by Meinders and Hanjalić (2002) for $Re_H \approx 3900$. The vertical mid-plane revealed a horseshoe vortex in front of the upstream prism and a recirculation region on its top surface. Visualizations of the instantaneous vorticity on two transverse mid-planes and in three dimensions indicated that the vortices around the prisms present a high degree of complexity and intensity, persisting far downstream while also interacting with one another. Some of these vortices resembled prototypical hairpin structures. The flow structures close to the front face of the downstream cube demonstrated a relatively high intensity. This observation was also confirmed by the energetic structures extracted from a POD analysis based on a total of 200 snapshots.

ACKNOWLEDGEMENTS

August 6th, 2017 marks the 4th year of my research work under supervision of Prof. Donald J. Bergstrom since the date I was in my 2nd year undergraduate. I would love to express my most sincere gratitude to Dr. Donald J. Bergstrom for not only being my professor but also being my mentor over the past years providing enlightenment, encouragement, and inspiration all the way along.

Simultaneously, I was very glad that I could attend many insightful courses instructed by Prof. David Sumner during my study here. His expertise enlightens me a lot on the experimental side of fluid mechanics

I would like to extend my thankfulness to Md Shakhawath Hossain for his patient guidance, and to Rajat Chakravarty, A S M Atiqul Islam and Mohammad Reza Haghgoo for all the helpful discussions we had during my M.Sc. program here.

I appreciate the invaluable friendship with Anurag Das, Minghan Chu and Hadi Hosseinzade Halqesari. They are reasons making my M.Sc. experience enjoyable.

Last but not least, I appreciate all the technical, and spiritual support Shawn Reinink has provided. His contribution is one of those reasons making my numerical work proceed very smoothly.

DEDICATION

To my beloved parents, Xiao and Yanxia, for all of your unwavering support.

You are the very reasons that I have made this far.

I love you all.

TABLE OF CONTENTS

LIST OF TABLES

LIST OF FIGURES

NOMENCLATURE

English symbols

A	coefficient of van Driest damping function
A_{ki}	k^{th} eigenvector
C_f	skin friction coefficient
c_s	speed of sound in lattice Boltzmann method (m/s)
C_s	constant for the standard Smagorinsky subgrid-scale model
D	spatial dimension (mm)
$\vec{e}_i$	discrete speed vectors
$\vec{F}$	external force field
f_i	particle distribution function
f_i'	post-collision particle distribution function
f_i^{eq}	equilibrium distribution
H	cubic prism height (mm)
I	identity matrix
i	streamwise position in the pre-cursor domain
$\vec{J}$	three-dimensional momentum field (kg·m/s)
j	spanwise position in the pre-cursor domain
k	wall-normal position in the pre-cursor domain

L_x	streamwise length of the target domain (mm)
L_y	spanwise length of the target domain (mm)
L_z	wall-normal height of the target domain (mm)
m	velocity moment
m^{eq}	equilibrium moment
M	transformation matrix
$\boldsymbol{M}$	number of snapshots
n	refinement factor
P	pressure (Pa)
Re_H	Reynolds number based on the cubic prism height
Re_m	Reynolds number based on the bulk velocity
Re_τ	Reynolds number based on the friction velocity
$\hat{S}$	diagonal collision matrix
S_{gap}	gap distance between cubic prims (mm)
S_i	relaxation rate
S_s	source term
$S_{i,j}$	strain rate tensor (s^{-1})
St	Strouhal number
δt	temporal step (s)
Δt_c	coarse grid temporal step (s)
Δt_f	fine grid temporal step (s)

tr	trace of the matrix
$\vec{U}$	three-dimensional velocity field (m/s)
U^+	normalized streamwise velocity using viscous length scale
U_{cl}	centerline velocity (m/s)
U_m	bulk velocity (m/s)
U_{max}	maximum streamwise velocity (m/s)
u_τ	friction velocity (m/s)
u	streamwise velocity component (m/s)
v	spanwise velocity component (m/s)
w	wall-normal velocity component (m/s)
$u_{i,j}$	velocity gradient tensor (m/s)
u'	streamwise fluctuation component (m/s)
v'	spanwise fluctuation component (m/s)
w'	wall-normal fluctuation component (m/s)
$\langle u \rangle$	streamwise mean velocity (m/s)
$\langle v \rangle$	spanwise mean velocity (m/s)
$\langle w \rangle$	wall-normal mean velocity (m/s)
$\langle u'u' \rangle^+$	normalized streamwise Reynolds stress using viscous length scale
$\langle u'w' \rangle^+$	normalized Reynolds shear stress using viscous length scale
X	coordinate in streamwise direction of the target domain
x	streamwise position in the target domain (mm)

δx	spatial step (mm)
Δ_x	reference length scale (mm)
Δx_c	coarse grid spacing (mm)
Δx_f	fine grid spacing (mm)
Δx^+	normalized streamwise grid spacing using viscous length scale
Y	coordinate in spanwise direction of the target domain
y	spanwise position in the target domain (mm)
Δy^+	normalized spanwise grid spacing using viscous length scale
Z	coordinate in wall-normal direction of the target domain
z	wall-normal position in the target domain (mm)
z^+	normalized wall-normal distance using viscous length scale
Δz^+	normalized wall-normal grid spacing using viscous length scale

Greek symbols

ϵ	empirical constant
λ_k	k^{th} eigenvalue
ν_c	coarse grid viscosity (m^2/s)
ν_f	fine grid viscosity (m^2/s)
ν_0	molecular viscosity (m^2/s)
ν_{SGS}	subgrid-scale viscosity (m^2/s)
ρ	fluid density (kg/m^3)

τ_w	wall shear stress (N/m^2)
Φ_k	k^{th} eigenfunction
ω_i	weighing factor
$\Omega_{i,j}$	vorticity tensor (s^{-1})

CHAPTER 1 INTRODUCTION

1.1 Motivation

Turbulent flow is characterized by its irregular and chaotic instantaneous patterns. The research of such flows is inherently complex and challenging, yet also relevant to many industrial and environmental applications. Computational fluid dynamics (CFD) is a powerful technique that analyzes a fluid flow and the associated phenomena by means of numerical simulation. It finds wide applications in industrial research and design, including fluid dynamics of aircraft, turbomachinery, chemical processing and meteorology (Versteeg and Malalasekra 2007).

Experimental approaches and computational simulations are two effective tools for studying turbulence. As compared with experimental fluid dynamics, CFD demonstrates several unique advantages including a reduction of effort in building the experimental environment, the capability to study large-scale systems, and the availability of data and flow information everywhere in the computational domain.

Traditionally, the governing equations in CFD are the Navier-Stokes equations. These 2^{nd} order nonlinear equations fundamentally determine macroscopic properties of the velocity and pressure fields in a fluid flow. The Navier-Stokes equations are nonlinear in nature and thus formidable to solve directly. Therefore, both computational techniques and theoretical models are required in solving these equations.

A novel numerical approach called the lattice Boltzmann method (LBM) has evolved over the past decades. Instead of solving the traditional Navier-Stokes equations, LBM seeks to perform the simulation through an algorithm that includes a collision model and a streaming process. This method demonstrates a relatively simple algorithm and is widely considered to be a potential alternative to the traditional methods adopted in CFD.

1.2 Literature review

The Lattice Boltzmann method (LBM) is a comparatively new and numerically efficient approach in computational fluid dynamics. It demonstrates the potential to become a promising alternative to the traditional Navier-Stokes equations and thus has found multiple applications in simulation of fluid flows (Yu 2004, Chikatamarla *et al.* 2010, Koda 2013, Hossain *et al*. 2015). The LBM is originally derived from the continuous Boltzmann equation through discretization in time and space, which describes a fluid system statistically based on the particle density distribution functions (He and Luo 1997). In fact, the Navier-Stokes equations for viscous flow can be recovered by applying the second-order Chapman-Enskog expansion to the continuous Boltzmann equation (Bespalko 2006). The LBM has also been mathematically characterized as a finite-difference-based scheme (He and Luo 1997, Yu 2004).

The flow field of the LBM consists of a number of fictitious particles moving along specified lattice directions at fixed velocities (Bespalko 2006). These particles collide and stream in a physical space that is discretized by a uniform grid. The macroscopic state at each lattice site can then be calculated from the corresponding particle distribution functions. Hence, implementation of the LBM involves two steps: collision and streaming. The collision process deals with their relaxation process to their local equilibrium, and the streaming process describes the movement of the particles along the specified directions to their neighbouring sites after the collision step (Premnath *et al.* 2009b). The LBM therefore demonstrates two key advantages over the traditional method: a simple algorithm and parallel scalability (Koda 2013). The former originates from the fact that there is no pressure solver involved in the algorithm to correct the velocity field; the pressure in the LBM is obtained from the local fluid density and the speed of sound.

Two collision models are widely used in the LBM: the single-relaxation-time (SRT) model and multiple-relaxation-time (MRT) model. The SRT is also referred to as the Bhatnager-Gross-Krook (BGK) model and has gained wide popularity for its simplicity in implementation (D'Humieres *et al.* 2002, Yu 2004). In the SRT-LBM, a single relaxation parameter essentially determines the rate at which the particle distributions relax to their local equilibrium, whereas the MRT model computes different relaxation rates in moment space (Premnath *et al.* 2009b). The

MRT LBM, also known as the generalized lattice Boltzmann method (GLBM), is generally preferred over the SRT LBM since it provides a higher numerical stability. This is especially the case for flows at high Reynolds numbers (Premnath *et al.* 2009b, Freitas *et al.* 2011). Additionally, optimal stability can be achieved by tuning the different relaxation rates individually (D'Humieres *et al.* 2002). The type of lattice models also has an impact on the capability of LBM. Several lattice models are particularly popular and widely employed for three-dimensional fluid flow simulation, including the three-dimensional, fifteen-particle velocity (D3Q15) lattice model, and models which are similarly described as D3Q19 and D3Q27. The number of velocity sites is one influencing factor to the numerical accuracy. However, a higher number of velocity sites typically also increases the computational load.

One major constraint imposed by the LBM in application to complex flows lies in its inherent uniformity in the computational domain. In order for the LBM to be effective in the exploration of complex fluid flows, this restriction should be circumvented. One effective approach to achieve this goal is local grid refinement. Over the past decades, a number of pioneering schemes have been proposed for local grid refinement. One early scheme proposed by He *et al.* (1996) is the interpolation-supplemented LBM. A continuously varying grid mesh is realized in this scheme where the values on the refined grid are simply obtained by interpolation from the coarse grid after each round of streaming and colliding. Filippova and Hanel (1998) proposed a popular scheme using the locally embedded grid. The entire computation domain is initially covered with the coarse grid. The fine grid is then patched to regions where turbulent eddy motions exist at small scales. Spatial and temporal interpolations are both implemented in this scheme to realize the communication between the coarse and the fine grids. Dupuis and Chopard (2003) developed a similar scheme to the one of Filippova and Hanel (1998), but using a simpler algorithm in interpolations with second-order accuracy. One common feature of the aforementioned schemes is that they are node-based, or finite-difference formulated, and interpolation of the surrounding nodes or rescaling serves as a critical step in implementing such local grid refinement. This approach does not inherently conserve mass, momentum and energy (Chen *et al.* 2006). One recent attempt to address this issue is the so-called imbalance correction grid refinement method proposed by Kuwata and Suga (2016). This approach is an extension to the work of Dupuis and Chopard (2003); a correction step is introduced to remove the unphysical discontinuity in the interface region serving to mitigate the non-conservation issue. Freitas *et al.*

(2006) developed a so-called hierarchical grid refinement. This refinement technique is also similar to the work of Filippova and Hanel (1998). However, one fundamental difference between them is that Freitas *et al.* (2006) used the cell-centered approach in their study and this makes it as a finite-volume-formulated scheme. In realizng this scheme, a non-linear interpoation is required along with a transformation of the non-equilibrium part of the distribution functions. Eitel-Amor *et al*. (2013) worked further on this scheme and developed a dynamic version of such local grid refinement called the hierarchical adaptive grid refinement. Instead of locating the refinement region manually, hierarchical adaptive grid refinement incorporates monitoring parameters in the scheme to determine the need of refinement for a region dynamically. In the study by Eitel-Amor *et al*. (2013), two dynamic parameters are used based on the absolute value of the vorticity vectors and the difference of the total pressure at low Mach numbers.

On the other hand, Chen *et al.* (2006) and Rohde *et al.* (2006) proposed a novel volumetrically formulated scheme. No interpolation is required to realize this local grid refinement while the laws of conservation are precisely satisfied in the grid transition. This scheme removes the extra steps in the algorithm associated with interpolation or rescaling. In addition, it removes the fact that the computational accuracy is directly related to the accuracy of the interpolation. The reduction in overall computational cost in this scheme is achieved by a factor of 16 for a coarse cubic grid (Premnath *et al.* 2013a). Fundamental explorations using classical turbulent channel flow based on this technique have demonstrated satisfactory results (Premnath *et al.* 2009(a, b)). Applications in complex flows using this technique (Premnath *et al.* 2013 (a, b) , Staubach 2013) have also yielded promising results. However, unphysical discontinuities are reported in some high-order statistics profiles (Rohde *et al.* 2006, Premnath *et al.* 2013a, Kuwata and Suga 2016). Athough the current limitation of the use of a uniform grid in the LBM has begun to be addressed over the previous decade, local grid refinement has not yet become a mature methodology. Therefore, additional studies are required to test and improve their predictive performance while ensuring the conservation laws are satisfied.

Large eddy simulation (LES) is a prevailing turbulence model that identifies two different eddy scales of turbulent flows through filtering: resolved-scale eddies with a length scale larger than the grid size and unresolved-scale eddies that are smaller than the grid size. LES computes the larger resolved-scale eddy motions by directly solving the governing equations without any *ad*

hoc assumption, and models the physical effects of the smaller unresolved-scale motions by using a subgrid-scale (SGS) model (Hou *et al.* 1996, Yu 2004). One such model is the standard Smagorinsky SGS model. This model has gained wide popularity over the past decades due to the fact that the turbulent eddy viscosity is based on a simple formulation using a strain-rate tensor. Incorporation of this traditional SGS model into the LBM was proposed early and demonstrated to be straightforward in implementation by Hou *et al.* (1996). It should be noted that significant differences exist in implementing LES based on the different governing equations. For the Navier-Stokes equations, the estimated eddy viscosity contributes to the evolution of the flow fields directly during the next time step, whereas for the LBM the eddy viscosity only alters the corresponding relaxation rates for the particle distribution functions which serve to specify the flow states (Yu 2004). Applications of LBM LES have been successfully implemented in many realistic flows (Yu 2004, Premnath *et al.* 2009a, Koda 2013, Hossain *et al.* 2015). However, such LBM LES has not yet been widely applied to the flow in wake regions where complex flow structures are expected.

1.3 Objectives

The present thesis will investigate the performance of LBM LES for studying turbulent near-wall flows. The research will begin with an in-house LBM code initially developed for micro-fluidic flows and later applied to simulation of a turbulent lid-driven cavity flow by Dr. Md. Shakhawath Hossain (Hossain *et al.* 2015). Three objectives are identified for the current research:

1. The first objective is to modify the in-house code to be able to predict turbulent wall-bounded channel flow. More specifically, it will be used to perform a Direct Numerical Simulation (DNS) of a turbulent channel flow for a low Reynolds number. The numerical results will be analyzed and compared to those of a well-documented study from the literature. Typical flow structures will also be studied.

2. A major limitation in applying the LBM to complex flows originates from the inherent uniformity of the grid over the computational domain. Therefore, the second objective of the current study is to improve the effectiveness of the LBM by implementing local grid

refinement. A laminar channel flow will be used for this investigation where the regions near the walls will be refined. The preliminary performance will be assessed by comparing the velocity profile to that of an analytical solution.

3. The third objective of the current research is to explore the capability of LBM LES in predicting the flow structures in a more complex flow than a typical channel flow. Geometric complexity will be increased by adding two cubic prisms on the bottom wall of the channel. A standard Smagorinsky SGS model will be incorporated in the framework of the LBM to realize an LES for this study. A pre-cursor inflow and a constant pressure are both required for the inlet and outlet boundary conditions, respectively. The three-dimensional coherent structures will also be analyzed using both of the second invariant criterion (Hunt *et al.* 1988) and a Proper Orthogonal Decomposition (Kim *et al.* 2005).

The scope of the current thesis will largely focus on the numerical methodology and its application to the turbulent channel flow and flow over wall-mounted cubes. A local grid refinement method will be introduced as an attempt to improve the potential application of the LBM to wall-bounded flows. However, due to the time constraint, the application will only be limited to a laminar channel flow. An LES based on a standard SGS model will be considered in this study. It will significantly enhance an in-house LBM code for performing LES of near-wall turbulent flows; however, it cannot address every feature of the LBM that could be potentially improved.

1.4 Thesis structure

The present thesis is organized as follows. The lattice Boltzmann method is introduced in Chapter 2 where the collision operator and lattice model employed in the current study are both described in detail. Chapter 2 also documents the boundary conditions, initial conditions, and the iterative algorithm for implementing the LBM code. A demonstration of volumetric grid refinement and its performance in a laminar channel flow is included in Chapter 2 as well.

Chapter 3 presents the LBM DNS of a turbulent channel flow where the performance of the developed code is validated by comparison to other results. The second invariant criterion is introduced in the same chapter to visualize the vortex structures.

The thesis then proceeds to demonstrate a LBM LES of the complex wake flow over two cubic prisms in Chapter 4. A standard Smagorinsky model is introduced as the SGS model. Both mean flow patterns and instantaneous flow structures are analyzed. A snapshot version of the POD (Kim *et al.* 2005) is also included to analyze the flow structures from a different perspective.

Finally, Chapter 5 identifies the conclusions drawn from the current research and provides views into the future work.

CHAPTER 2 LATTICE BOLTZMANN METHOD

2.1 Background

The current research essentially employs a MRT collision model to study three-dimensional turbulent flows based on a D3Q19 lattice model. This chapter aims to provide a detailed description of the numerical methodology and thereby is organized as follows. The MRT LBM and D3Q19 lattice model are presented in Section 2.2 and Section 2.3. The chapter then proceeds by describing the different boundary conditions, initial conditions and external forcing terms employed in the current study, in Sections 2.4 and 2.5. The implementation algorithm for the newly developed LBM code is discussed in Section 2.6. Finally, a detailed description of the selected local grid refinement method is given in Section 2.7, along with a preliminary performance test using a laminar channel flow.

2.2 Multiple Relaxation Time LBM

The evolution equation for the MRT LBM is given by (Yu 2004):

$$f(\vec{x} + \vec{e}\delta t, t + \delta t) - f(\vec{x}, t) = -M^{-1} \times \hat{S} \times [m - m^{eq}], \quad (2.1)$$

where $f(\vec{x}, t)$ represents the particle distribution function, and $f(\vec{x} + \vec{e}\delta t, t + \delta t)$ is a particle distribution function that describes the corresponding particle movement for the next time step, δt, to the neighbouring lattice node, δx, along a specified direction, $\vec{e}$. Equation (2.1) is written using the convention that the LHS of the equation denotes the streaming process whereas the RHS signifies the cumulative effect of the collision process. $\hat{S}$ stands for the diagonal collision matrix that determines the relaxation rates and is given by:

$$\hat{S} = diag\ (S_1, S_2, S_3, S_4, S_5, S_6, S_7, S_8, S_9, S_{10}, S_{11}, S_{12}, S_{13}, S_{14}, S_{15}, S_{16}, S_{17}, S_{18}, S_{19}). \quad (2.2)$$

The detailed values of the above diagonal matrix are provided in Appendix .

In equation (2.1), M is a 19 × 19 matrix that linearly transforms the distribution functions into velocity moments (Yu 2004):

$$m(x,t) = M \times f(x,t), \text{and } f(x,t) = M^{-1} \times m(x,t), \tag{2.3}$$

where the elements of M and M^{-1} are given in Appendix . The equilibrium moments in equation (2.1), m^{eq}, are functions of density and local velocities, details of which are specified in Appendix as well.

The fluid density and momentum in LBM are given by

$$\rho = \sum_{i=0}^{18} f_i \text{ , and } \rho\vec{U} = \sum_{i=0}^{18} \vec{e_i} f_i . \tag{2.4a, b}$$

The sound speed is $c_s = c/\sqrt{3},$ and $c = \delta x/\delta t = 1$ in lattice units. Physically, $\delta x =$ 0.001 m and $\delta t = 0.001$ s, respectively. The molecular viscosity is given by

$$\nu_0 = \frac{c}{3}\left(\frac{1}{s_\nu} - \frac{1}{2}\right)\delta x, \tag{2.5}$$

where $s_\nu = s_{10} = s_{12} = s_{14} = s_{15} = s_{16}$. In the current study, $s_\nu = 1.98570$ such that $\nu_0 = 1.20 \times 10^{-6}$ m^2/s.

The equilibrium distribution function for the LBM is given by

$$f_i^{eq} = \rho\omega_i\left[1 + 3\left(\vec{e_i}\cdot\vec{U}\right) + \frac{9}{2}\left(\vec{e_i}\cdot\vec{U}\right)^2 - \frac{3}{2}u^2\right], i = 0, 1, 2, \ldots, 18, \tag{2.6}$$

where ρ is the fluid density, ω_i and $\vec{e_i}$ are the weighting factors associated with the lattice model, and discrete velocity vectors, respectively. Both of them are specified in Section 2.3 below. In equation 2.6, $\vec{U} = \vec{U}(u(x,y,z), v(x,y,z), w(x,y,z))$ is the initial three-dimensional velocity field where *u*, *v* and *w* are velocity components at different locations in the domain.

2.3 D3Q19 lattice model

The D3Q19 lattice model has a total of nineteen discrete velocities. The corresponding discrete vectors are given by

$$\overrightarrow{e_i} = \begin{cases} (0,0,0), & i = 0; \\ (\pm 1,0,0),(0,\pm 1,0),(0,0,\pm 1) & i = 1,2,\dots,6; \\ (\pm 1,\pm 1,0),(\pm 1,0,\pm 1),(0,\pm 1,\pm 1) & i = 7,8,\dots,18. \end{cases}$$

The values of the weighting factors, ω_i, are dependent on the lattice model. For the D3Q19 lattice model, they are specified as

$$\omega_i = \begin{cases} \frac{1}{3}, & i = 0; \\ \frac{1}{18}, & i = 1,2,\dots,6; \\ \frac{1}{36}, & i = 7,8,\dots,18. \end{cases}$$

Graphically, the D3Q19 model is depicted in Figure 2.1

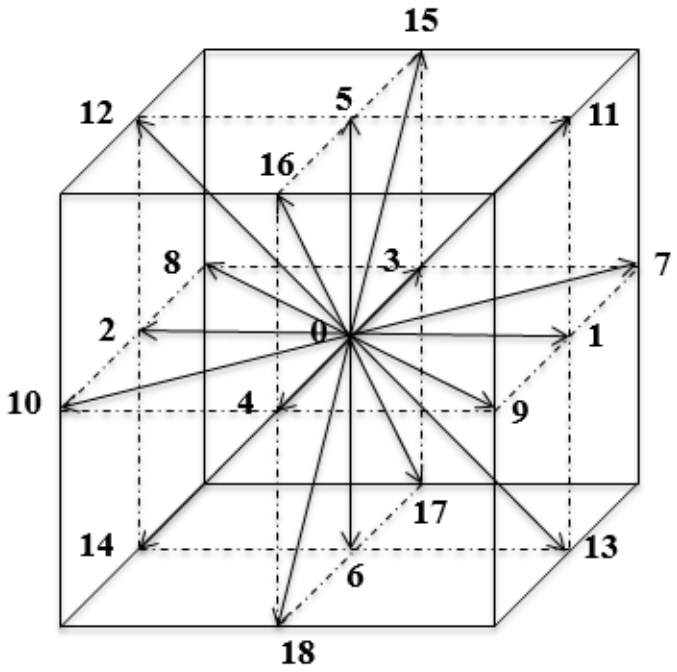

Figure 2.1. D3Q19 lattice model

2.4 Boundary conditions

When the particles reach the boundaries of the computational domain after streaming and collision, information on the particle density distribution functions is not provided for the next time step. Boundary conditions, therefore, serve to provide the unknown information for the distribution functions, thus meeting the constraints imposed along the boundaries. Four types of LBM schemes are introduced in the current study to realize different boundary conditions. They are presented in detail in the following subsections.

2.4.1 Halfway bounce-back boundary condition

The halfway bounce-back scheme realizes the no-slip boundaries at solid walls. It represents second-order accuracy for plane walls and first-order accuracy for curved boundaries (He *et al.* 1997, Freitas *et al.* 2011). This scheme is named “halfway bounce-back” since the exact

no-slip location is implemented halfway between the fictitious boundary node and the first inner node by simply “bouncing back” the incoming particles to their opposite directions, i.e.

$$f_0' = f_0\,, \qquad f_1' = f_2, \qquad f_2' = f_1, \qquad f_3' = f_4, \qquad f_4' = f_3,$$

$$f_7' = f_{10}, \qquad f_8' = f_9, \qquad f_9' = f_8, \qquad f_{10}' = f_7,$$

$$f_5' = f_6, \qquad f_{11}' = f_{14}, \qquad f_{12}' = f_{13}, \qquad f_{15}' = f_{18}, \qquad f_{16}' = f_{17},$$

$$f_6' = f_5, \qquad f_{13}' = f_{12}, \qquad f_{14}' = f_{11}, \qquad f_{17}' = f_{16}, \qquad f_{18}' = f_{15},$$

where f_n' and f_n denote the post-collision particle distribution functions and distribution functions of the previous time step after the streaming process, respectively. Note that the boundary nodes on the solid walls do not participate in the collision process. Graphically, this scheme is presented in Figure 2.2. Note that the lattice model in this study employs D3Q19, but D2Q9 is the one demonstrated in Figure 2.2 for simplicity while not losing generality.

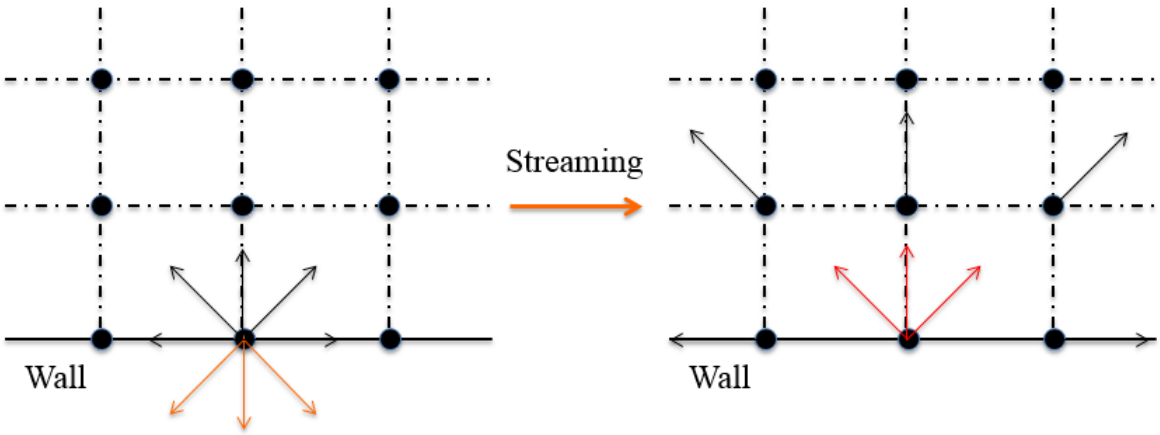

Figure 2.2. Half-way bounce-back boundary condition

2.4.2 Periodic boundary condition

A periodic boundary condition essentially connects the inlet and outlet in the specified direction such that the fluid flow in the domain follows a periodic pattern. This condition is simply realized by connecting the lattice nodes at the outlet to the corresponding lattice nodes at the inlet. Consequently, no single particle leaves the computational domain and the laws of conservation are well preserved. When a periodic boundary condition is applied, a sufficiently large domain should be used such that there is negligible statistical correlation between any two points separated by a distance equal to half of the computational domain (Rohde *et al.* 2006).

2.4.3 Precursor inlet boundary condition

A precursor inlet boundary condition provides an instantaneous inlet velocity profile for the downstream domain by extracting the velocity profile at each time step from an upstream periodic quasi-steady-state flow. This boundary condition is implemented by providing the distribution functions at the downstream inlet plane with velocity information at the upstream outlet, and density of the first inner nodes in the downstream domain, i.e. (Koda 2013)

$$f_i = f_i^{\mathrm{eq}}\left(\rho(x+1,y,z), \vec{U}(i,j,k)\right), \tag{2.7}$$

where f_i and f_i^{eq} represent the particle distribution functions and equilibrium distribution functions at the inlet plane of the downstream domain, respectively. Here $\rho(x+1,y,z)$ denotes the density of the first inner nodes in the downstream domain, and $\vec{U}(i,j,k)$ stands for the instantaneous velocities at the upstream outlet. A schematic diagram and details of the application are included in Section 4.3.

2.4.4 Constant pressure outlet boundary condition

The pressure at the outlet, P_{out}, is maintained as constant via setting the density as constant, $\rho_{\text{out}} = \text{constant}$, since in the LBM $\rho_{\text{out}} = P_{\text{out}}/{c_s}^2$. Therefore, the particle distribution functions at the outlet need to be modified as follows (Mussa *et al.* 2009):

$$f_i = f_i^{eq}\left(\rho_{\text{out}}(x,y,z), \vec{U}(x-1,y,z)\right), \tag{2.8}$$

where $\vec{U}(x-1,y,z)$ denotes the velocity field of the last inner nodes prior to the outlet plane of the target domain.

2.5 External force

The current LBM scheme incorporates a source term in the equations for the particle distribution functions to simulate the effect of a pressure gradient to drive the fluid flow. With the source term added, the evolution equation takes the form of (Premnath *et al*. 2009a)

$$f(\vec{x}+\vec{e}\delta t, t+\delta t) - f(\vec{x},t) = -M^{-1}\times\hat{S}\times[m-m^{eq}] + M^{-1}\times\left(I-\frac{1}{2}\hat{S}\right)\times S_s, \tag{2.9}$$

where the second term on the RHS of the above equation (2.9) introduces the effects of the pressure gradient. I is a 19×19 identity matrix and S_s denotes the source term in moment space, the components of which are specified in Appendix.

A corresponding forcing term is also introduced in the relation for the local momentum field, i.e.

$$\vec{j} = \rho\vec{U} = \sum_{i=0}^{18} f_i\vec{e_i} + \frac{1}{2}\vec{F}\delta_t, \tag{2.10}$$

where $\vec{j} = \vec{j}(j_x, j_y, j_z)$ is the momentum field, $\vec{U}$ denotes the local velocity field and $\vec{F} = \vec{F}(F_x, F_y, F_z)$ represents the external force field. Note that the source term involved in the evolution

equation (2.9) is essentially a function of the external force, $\overrightarrow{F}$, and local velocity, $\overrightarrow{U}$. For the turbulent channel flow, the external force field is determined by (Jafari *et al.* 2014)

$$F_x = -\frac{dP}{dx} = \frac{8\tau_w}{L_z} = \frac{8\rho {u_\tau}^2}{L_z}, F_y = 0, F_z = 0, \tag{2.11}$$

In equation 2.11, dP/dx is the pressure gradient, τ_w is the wall shear stress, L_z denotes the channel height, and u_τ is the friction velocity.

2.6 Initial condition

A sinusoidal perturbation, superimposed on a one-seventh power law for the mean velocity profile in all three dimensions, serves as the initial condition for the fluid flow in the current study. These perturbations attempt to trigger turbulence in the early stage of development. Note that the initial condition does not affect the quasi-steady state; the initial state only serves to reduce the computational effort it takes to reach the fully developed state. Mathematically, the perturbations are expressed as (Lam 1989)

$$u' = \epsilon L_x \sin\left(\frac{\pi z}{L_z}\right)\left(\cos\frac{2\pi x}{L_x}\sin\frac{2\pi y}{L_y} + \frac{1}{2}\cos\frac{4\pi x}{L_x}\sin\frac{2\pi y}{L_y} + \cos\frac{2\pi x}{L_x}\sin\frac{4\pi y}{L_y}\right), \tag{2.12}$$

$$v' = -\epsilon L_y \sin\left(\frac{\pi z}{L_z}\right)\left(\frac{1}{2}\sin\frac{2\pi x}{L_x}\cos\frac{2\pi y}{L_y} + \frac{1}{2}\sin\frac{4\pi x}{L_x}\cos\frac{2\pi y}{L_y} + \frac{1}{4}\sin\frac{2\pi x}{L_x}\cos\frac{4\pi y}{L_y}\right), \tag{2.13}$$

$$w' = -\epsilon\left(1 + \cos\frac{\pi z}{L_z}\right)\left(\sin\frac{2\pi x}{L_x}\sin\frac{2\pi y}{L_y} + \sin\frac{4\pi x}{L_x}\sin\frac{2\pi y}{L_y} + \sin\frac{2\pi x}{L_x}\sin\frac{4\pi y}{L_y}\right), \tag{2.14}$$

where u', v' and w' represent the sinusoidal fluctuations in the streamwise (*X*), spanwise (*Y*) and wall-normal (*Z*) directions, respectively. Note that *x*, y, and z signify the corresponding locations in the *X*, *Y*, and *Z* directions. L_x, L_y and L_z denote the total length of the computational domain in the *X*, *Y* and *Z* directions. ϵ is an empirical constant determining the magnitude of the perturbations

and, in the current study, is set to $\epsilon = 3.65 \times 10^{-5}$. Note that an inappropriate ϵ value may result in divergence or delaying triggering of turbulence.

Consequently, the three components of the velocity field in the equilibrium distribution functions (Eqn. 2.6) become

$$u = \langle u \rangle + u', v = \langle v \rangle + v', w = \langle w \rangle + w',$$

where, for turbulent channel flow, $\langle u \rangle$ is the streamwise velocity determined using the one-seventh power law, and $\langle v \rangle = \langle w \rangle = 0$.

2.7 Implementation of the LBM code

The iterative steps for implementing the basic LBM algorithm are as follows:

1) Initial conditions

This step defines the relevant parameters and variables, specifies the computational domain, and determines the macroscopic properties, etc.

2) Equilibrium distribution functions

This step specifies the initial state of the fluid flow. The initial conditions of the fluid velocity field and the perturbations are implemented in this step.

3) Collision process

The external force that simulates the pressure gradient driving the flow is implemented in this step. Note that the wall nodes where no-slip boundary conditions are applied do not participate in this step.

4) Boundary conditions

5) Streaming step

Particles propagate from one node to the neighbouring site in this step.

Back to step 3) until quasi-steady state developed.

6) **Post-processing subroutines**

Subroutines in this step process the data sets for analysis and visualization after reaching the quasi-steady state.

2.8 Local grid refinement

This subsection studies the volumetric local grid refinement proposed by Chen *et al.* (2006) and Rohde *et al.* (2006). This approach is preferred over other schemes because it is a finite-volume-based scheme and presents promising results while involving a comparatively simple algorithm. A locally refined laminar channel flow is simulated in this subsection to test the basic performance of this refinement scheme. The results will be compared to the analytical solution.

2.8.1 Volumetric grid refinement

Implementation of volumetrically formulated grid refinement relies on the volumetric description of the LBM. This concept is illustrated in Figure 2.3. Rather than the original particle distribution function on each lattice node, it is the mass distribution function on each cell that is now under consideration. Within each single cell volume, particle densities are assumed to be uniform everywhere. This re-interpretation of LBM results in a staggered grid arrangement schematically shown in Figure 2.4. One character of volumetric grid refinement that distinguishes itself from the other schemes is that the fine grid cell (Cell B in Figure 2.3) and the coarse grid cell (Cell A in Figure 2.3) do not share the identical spatial or temporal scales. These scales are proportionally associated with the grid refinement factor, n, such that spatially $\Delta x_c = n\Delta x_f$ and temporally $\Delta t_c = n\Delta t_f$ where f and c denote the fine grid and coarse grid, respectively (Rohde *et al.* 2006).

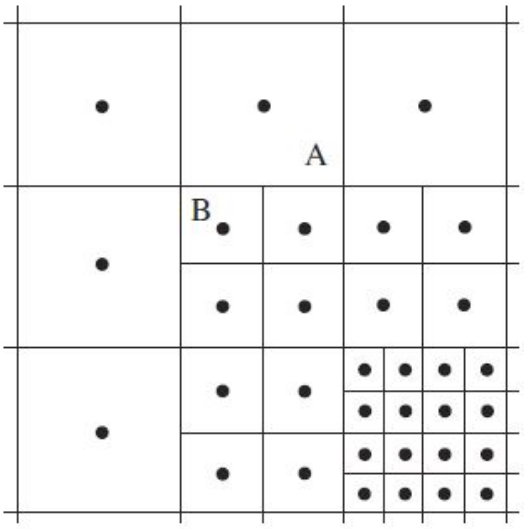

Figure 2.3 Finite-volume grid refinement based on volumetric LBM (Rohde *et al.* 2006)

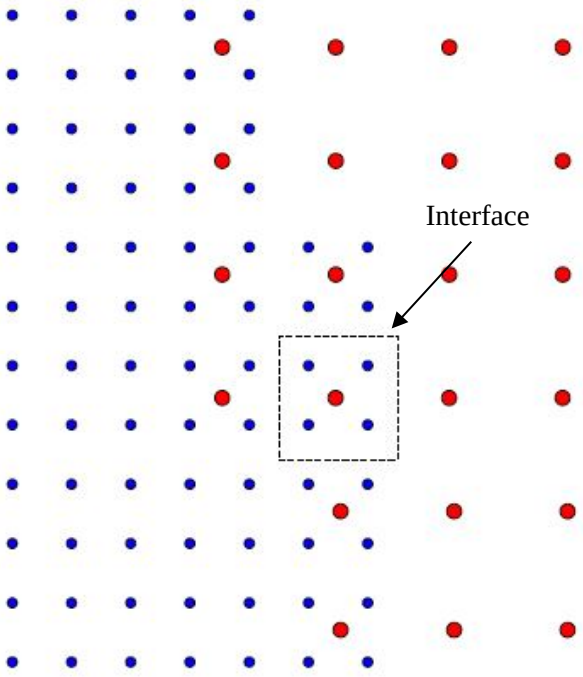

Figure 2.4. Staggered grid arrangement for local grid refinement (Premnath *et al.* 2013a)

During the computation, the fine grid covers the regions where turbulent structures at small scales exist, i.e. near-wall regions and regions in proximity to surface geometry. The rest of the domain is taken care of by the coarse grid where fairly large structures are expected. There exists a single interface layer shown in Figure 2.4 where both grids overlap, serving the role of communication between the two grids. Two critical steps are implemented for this interconnection: explode and coalesce. The former deals with the transition from the coarse grid to the fine grid, and the latter works the other way around. In the explode step, the information on the post-collision state for the coarse grid in the interface is uniformly redistributed to the fine grid. Conversely, in the coalesce step, the pre-collision state fine grid in the interface layer provides the input for the corresponding coarse grid (Chen *et al*. 2006). Note that these two steps, explode and coalesce, are implemented only on the directions pointing into the fine grid and the coarse grid, respectively (Rohde *et al.* 2006).

2.8.2 Algorithmic steps

The detailed algorithmic steps implemented for local grid refinement are specified below following Chen *et al*. (2006) and Rohde *et al*. (2006):

1) Explode

Over the interface, mass distribution in a coarse grid cell is uniformly redistributed into a number of n^D fine grid cells, with n denoting the refinement factor and D the spatial dimension. Normally n is an even number and in this case, $n = 2$ and $D = 3$. This process is graphically illustrated in Figure 2.5. Note that the densities do not change and are assumed to be uniform anywhere. No interpolation or rescaling is required here.

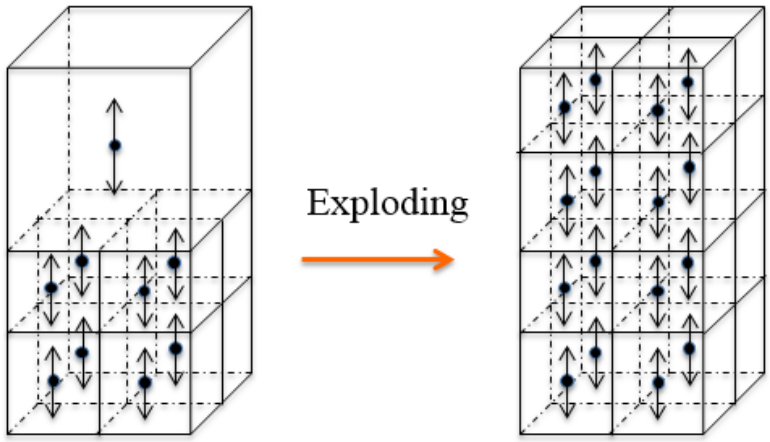

Figure 2.5. Graphical illustration of explode

2) **Standard streaming step on the fine nodes**

3) **Standard collision step on the fine nodes**

The collision step is performed on the fine nodes for this step along with the external force, if there is any. Note that this step is not performed on the fine nodes located in the overlap region.

4) **Application of wall boundary conditions on the current grid level**

5) **Repeat steps 2) to 4) *n*-1 times**

It should be reiterated that the fine grid and the coarse grid do not share the identical spatial or temporal scales; these scales are related to *n* such that $\Delta x_c = n\Delta x_f$ and $\Delta t_c = n\Delta t_f$. Therefore, in this case, the fine grid takes two time steps for each time step taken by the coarse grid in each iteration.

6) **Standard streaming step on the coarse nodes**

7) **Coalesce**

This step is the converse of the explode step; summation of the mass distribution on the fine cells to provide information for the corresponding coarse cell over the interface region.

Again, note that neither interpolation nor rescaling is performed in this step. Graphically, this step is shown in Figure 2.6 below

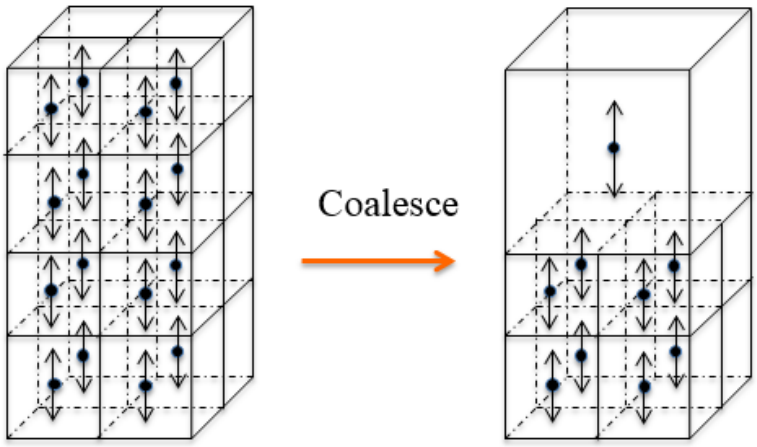

Figure 2.6. Graphical illustration of coalesce

8) **Standard collision step on the coarse nodes**

9) **Back to step 1)**

2.8.3 Performance of local grid refinement

Exploration of the volumetric local grid refinement started with a numerical validation using a fully developed laminar channel flow. A creeping laminar flow in the wall-bounded channel with a Reynolds number of $Re = U_{cl}(L_z/2)/\nu_0 \approx 1.08$ was considered; U_{cl}, L_z and υ_0 here denote the centerline velocity, channel height and molecular viscosity, respectively. No-slip boundary conditions were applied to the top and bottom walls using the halfway bounce-back scheme. Periodic boundary condition was realized in the streamwise and spanwise directions, respectively. An external force simulating the effect of pressure gradient was used to drive the flow. Details are provided in Section 2.5 in terms of modifying the particle distribution functions to incorporate the external force field.

Two grid resolutions, i.e. $n = 2$, were implemented in the computational domain where the coarse grid was applied in the center, and regions near the walls were refined using the fine grid. The height of each of the fine grid layers is 14 fine unit cells, which is 7 coarse unit cells. Meanwhile, since $\nu_0 = (1/3)((1/s_\nu) - (1/2))c\delta x$ for the coarse grid, the corresponding relaxation parameters related to the molecular viscosity on the fine grid were adjusted such that the viscosities match on both grids, i.e. $\nu_c = (1/n)\nu_f$. The corresponding numerical specifications are summarized in Table 2.1 and the computational domain is illustrated in Figure 2.7.

A plot of the predicted velocity profile is presented in Figure 2.8. The laminar velocity profile agrees very well with its analytical solution. Slight discrepancies are observed at two locations: under-estimation in proximity to the wall and over-estimation in the overlap region. The former originates from the halfway bounce-back scheme, and the latter could be due to the transfer of the numerical information. This over-estimation is quantified as 2.89% in this case by comparison with the analytical solution. A non-physical discontinuity is not observed here.

The current simulation of laminar channel flow only serves as a preliminary test of the performance of the local grid refinement method. Further testing is required and could be performed using turbulent channel flow. Note that in turbulent channel flow, the grid resolution used here is not sufficiently fine to capture the turbulence perfectly well. But lower-order turbulence statistics profiles are expected to match well with the documented results.

Table 2.1. Specifications of computational domain

	Coarse grid	**Fine grid**
Computational domain $L_x \times L_y \times L_z$:	128 × 64 × 64	256 × 128 × 128
Coarse grid size	128 × 64 × 50	-
Fine grid size (top and bottom walls)	-	256 × 128 × 14
Molecular viscosity (m^2/s)	1.2×10^{-6}	2.4×10^{-6}
Density (kg/m^3)	1.0	1.0
External force factor	3.726×10^{-7}	1.863×10^{-7}

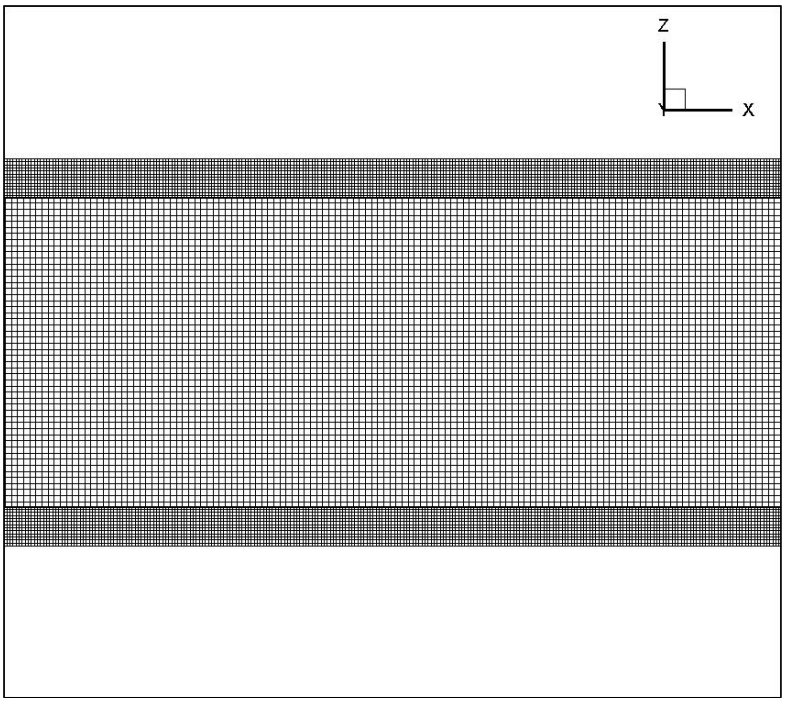

Figure 2.7. Wall-bounded channel (*X*: streamwise direction; *Y*: spanwise direction; *Z*: wall-normal direction)

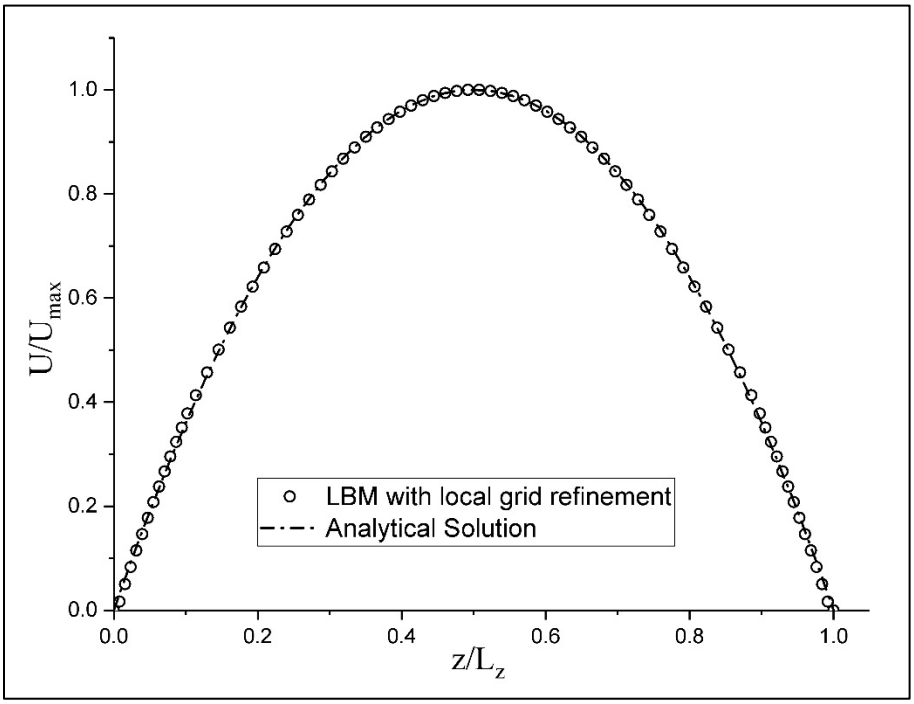

Figure 2.8. Velocity profile for laminar channel flow

CHAPTER 3 LBM DNS OF TURBULENT CHANNEL FLOW

3.1 Background

Turbulent channel flow is a typical benchmark case in fluid mechanics that has been studied extensively, partly because it provides understanding of the basic physics of wall-bounded turbulence and due to its geometric simplicity. The code developed in the current study will be validated by comparing the mean flow variables and lower-order statistics with those of a turbulent channel flow investigated by Kim *et al.* (1987) via DNS based on the Navier-Stokes equations.

Kim *et al.* (1987) studied this flow using a mesh size of 192 × 160 × 129 in the streamwise (X), spanwise (Y) and wall-normal (Z) directions, respectively. A Reynolds number of $Re_\tau = u_\tau(L_z/2)/\nu_0 \approx 180$ was realized in their simulation, where u_τ is the friction velocity and L_z is the channel height. They applied periodic boundary conditions to the streamwise and spanwise directions, and the no-slip boundary conditions to the top and bottom walls, respectively. The grid spacing in the streamwise and spanwise directions was $\Delta x^+ \approx 12$, and $\Delta y^+ \approx 7$, respectively. A non-uniform mesh was employed in the wall-normal direction with the first inner node located at $z^+ \approx 0.05$. In the center of the channel, $\Delta z^+ \approx 4.4$. The numerical study of Kim *et al.* (1987) has been validated by comparison with experiments and has served as a benchmark for evaluating the quality of other numerical simulations of turbulent channel flow, though slight discrepancies were recognized in the comparisons of higher-order statistics profiles.

This chapter aims to validate the predictions of the LBM code for a turbulent channel flow from different perspectives and is organized as follows. The computational specifications of the current simulation will be introduced in Section 3.2, followed by the data comparison using the mean flow variables, the velocity profiles and Reynolds stress profiles in Section 3.3. Data visualizations will then be presented and discussed in Section 3.4.

3.2 Computational specifications

The current simulation was realized using a grid size of 396 × 105 × 198 in the *X*, *Y* and *Z* directions, respectively. The grid was uniformly configured in all three directions, and the spacing in wall units was $\Delta^+ \approx 2.38$. The first inner node in the wall-normal direction was located at $\Delta z^+ \approx 1.19$. Periodic boundary conditions were applied in the streamwise and spanwise directions, and no-slip boundary conditions were realized at the top and bottom walls using a halfway bounce-back scheme. A Reynolds number of $Re_\tau = u_\tau(L_z/2)/\nu_0 \approx 230$ was achieved in the current simulation, slightly higher than that of Kim *et al.* (1987). Though this difference does yield a slightly stronger turbulence field, it is possible to make explicit comparisons using the normalized results. The fluid flow initially started with a predetermined mean velocity profile based on the one-seventh power law. Sinusoidal perturbations were superimposed in all three directions. The relevant details of the initial conditions are specified in Section 2.5. An external forcing term was employed to simulate the effects of a pressure gradient to drive the flow. It should be reiterated that the initial perturbations do not affect the fully-developed state of the fluid flow; they essentially serve to expedite the development of turbulence. The time-averaged quantities in the following sections are all based on the mean values calculated over 174,000 time steps after the flow had reached a quasi-steady state.

3.3 Mean flow properties

The mean flow variables of the current simulation are summarized in Table 3.1 along with those of the study by Kim *et al.* (1987). Given that the current DNS of turbulent channel flow represents a slightly higher Reynolds number, the mean flow variables of two studies agree well with one another. Meanwhile, the ratio of the centerline velocity to bulk velocity, U_{cl}/U_m, and the skin friction coefficient, C_f, of the current study also match well with the correlations suggested by Dean (1978), i.e.

$$\frac{U_{cl}}{U_m} = 1.28 {Re_m}^{-0.0116}, \tag{3.1}$$

$$C_f = 0.073 {Re_m}^{-0.25}, \tag{3.2}$$

where Re_m is the Reynolds number based on the bulk velocity and the entire channel height, L_z. The bulk velocity is calculated based on the streamwise mean velocity, $\langle u \rangle$, i.e.

$$U_m = \frac{1}{2}\int_0^2 \langle u \rangle \, d\left(\frac{z}{L_z/2}\right). \tag{3.3}$$

Table 3.1. Mean flow results for turbulent channel flow

	Kim *et al.* (1987)	**Current study**	**Dean (1978)**
$Re_\tau = \frac{u_\tau(\frac{L_z}{2})}{\nu_0}$	180	230	-
$\frac{U_m}{u_\tau}$	15.63	16.76	-
$\frac{U_{cl}}{u_\tau}$	18.20	19.83	-
$\frac{U_{cl}}{U_m}$	1.16	1.18	1.15
$C_f = \frac{\tau_w}{\frac{1}{2}\rho {U_m}^2}$	8.18×10^{-3}	7.12×10^{-3}	7.76×10^{-3}

Figures 3.1(a) and 3.1(b) present the streamwise mean velocity profiles as a function of wall normal distance normalized by the viscous length scale and channel half-height, respectively. The mean velocity profile in wall units of the current DNS agrees well with both of the canonical logarithmic law and the profile of Kim *et al.* (1987). The current mean velocity plotted against the normalized coordinate ($z/(L_z/2)$) sits higher than the profile of Kim *et al*. (1987). This difference largely originates from the higher Reynolds number in the current study.

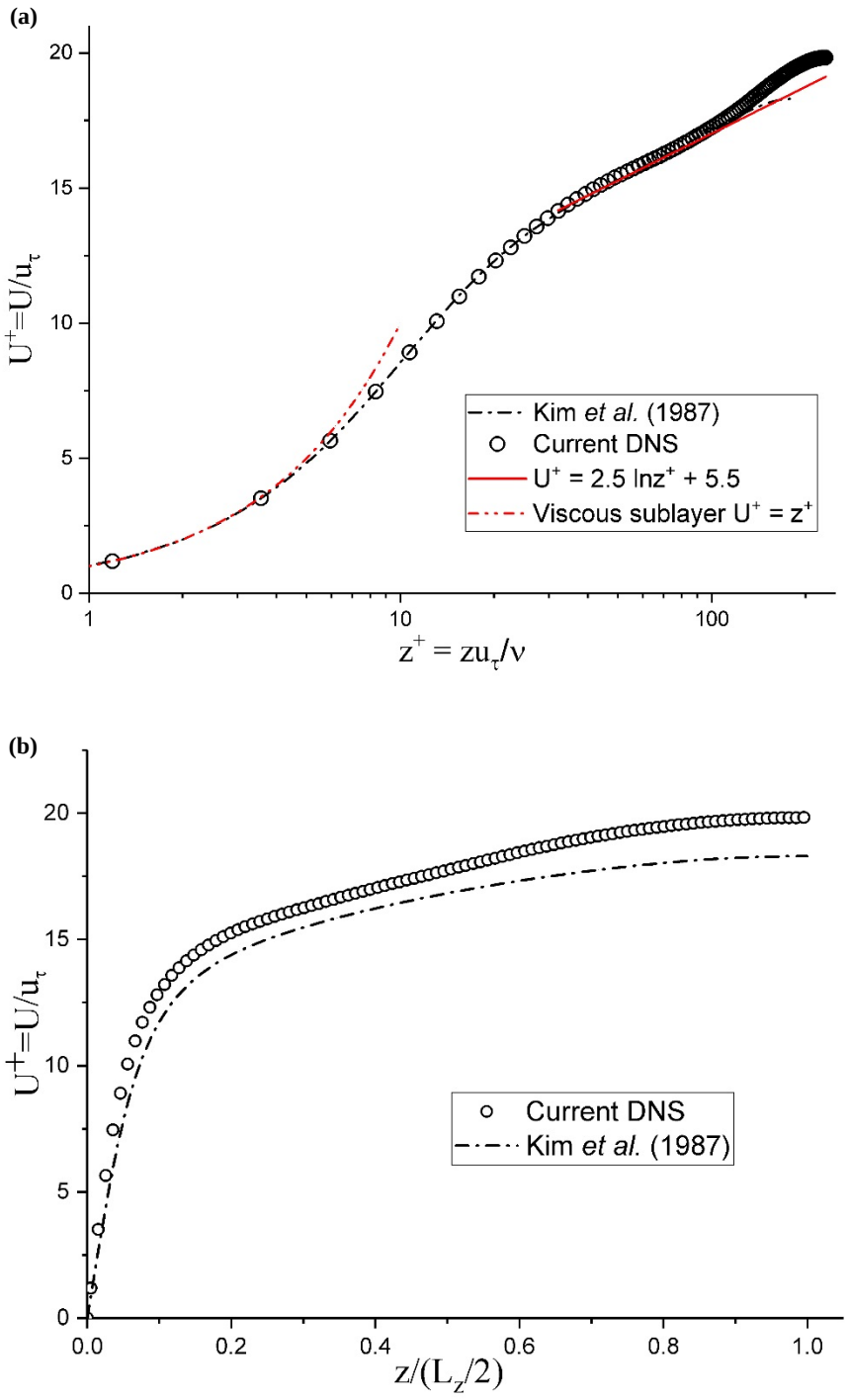

Figure 3.1. (a) Velocity profiles normalized using viscous length scale; (b) Velocity profiles normalized using half-channel height

Two normalized Reynolds stress profiles, i.e. $\langle u'u' \rangle^+$ and $\langle u'w' \rangle^+$, are presented in Figures 3.2(a) and 3.2(b), respectively. These stresses represent the horizontal and vertical flux of streamwise turbulent momentum. Mathematically, based on the DNS data sets, these two terms are evaluated as follows:

$$\langle u'u' \rangle^+ = \langle u'u' \rangle / {u_\tau}^2 = (\langle uu \rangle - \langle u \rangle \langle u \rangle) / {u_\tau}^2, \tag{3.4}$$

$$\langle u'w' \rangle^+ = \langle u'w' \rangle / {u_\tau}^2 = (\langle uw \rangle - \langle u \rangle \langle w \rangle) / {u_\tau}^2, \tag{3.5}$$

where $\langle \quad \rangle$ signifies time-averaging operation, $u = \langle u \rangle + u'$ and $w = \langle w \rangle + w'$. Both stress profiles are in reasonably good agreement with the reference values (at a lower Reynolds number). The slight over-predictions observed, especially in terms of the peak values, are believed to arise from the difference in Reynolds numbers. On the other hand, due to the comparatively coarse grid in proximity to the wall, the friction velocity was slightly inaccurate. This also contributes to the discrepancy in the Reynolds stress profiles. Based on the comparisons, the grid resolution employed was sufficient to predict the 2nd order statistics profiles reasonably well.

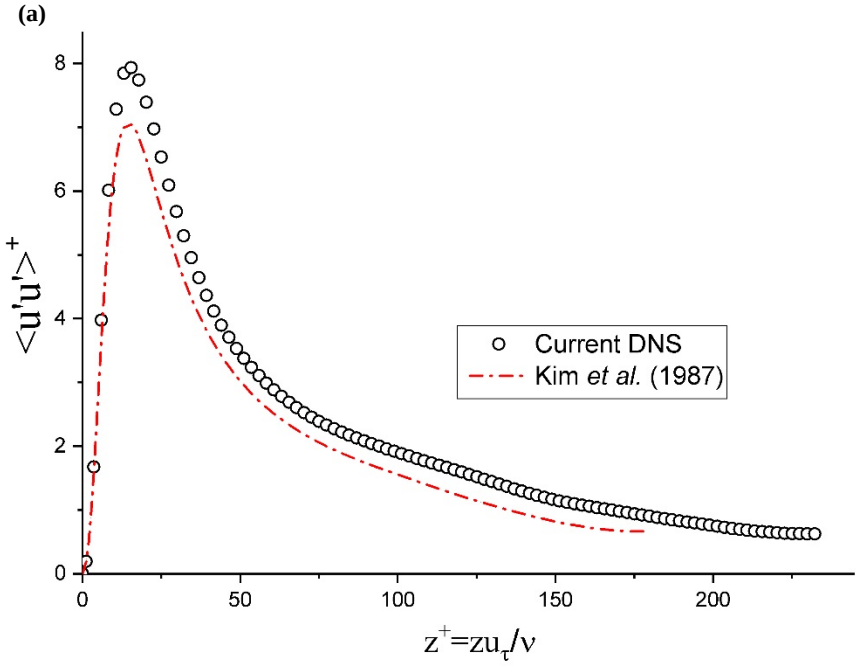

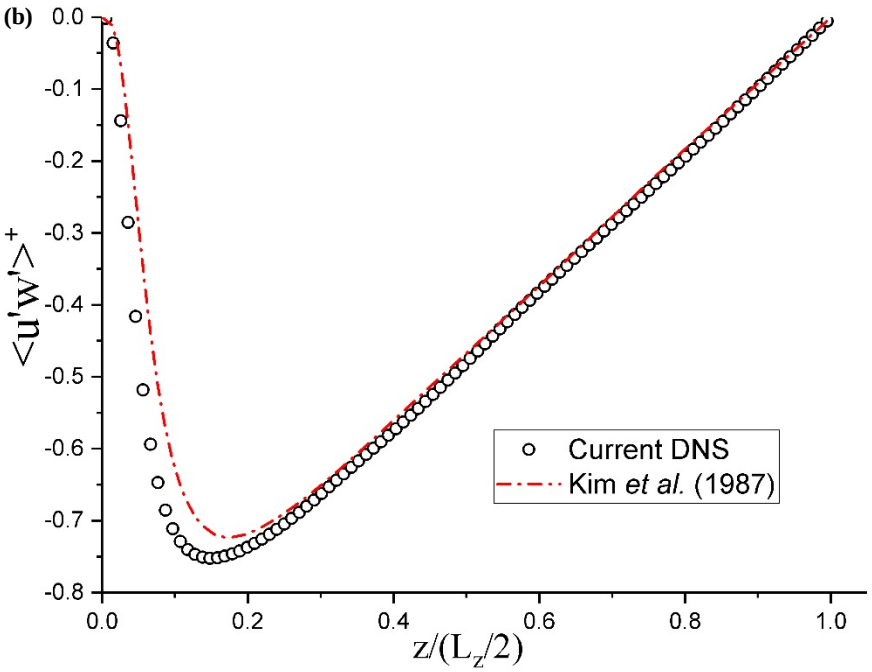

Figure 3.2. (a) The streamwise normal Reynolds stress; (b) The Reynolds shear stress

3.4 Near-wall structures

Elongated streaks of fluid with low streamwise velocity are observed in Figure 3.3 at an *X*-*Y* plane located at $z^+ = 8.5$. Figure 3.4 shows the instantaneous in-plane vorticity at four individual *X*-*Z* cross-sections. Strong vortices are identified in the near-wall regions as expected. Both the intensity and magnitude of the vorticity increases in the vicinity of the walls. Near the centerline, larger vortex structures are clearly identified.

Figure 3.5 visualizes the instantaneous vortex structures in the turbulent channel flow using the second invariant criterion. The second invariant criterion, or *Q* criterion, is a popular criterion for identifying a local fluid region as a vortex, i.e. vorticity is dominant when $Q > 0$ (Hunt *et al.* 1988). This concept could be illustrated using an expression by (Jeong and Hussain 1995):

$$Q \equiv \frac{1}{2}\left(u_{i,j}^2 - u_{i,j}u_{j,i}\right) = -\frac{1}{2}u_{i,j}u_{j,i} = \frac{1}{2}\left(\left\|\Omega_{i,j}\right\|^2 - \left\|S_{i,j}\right\|^2\right) > 0, \qquad (3.6)$$

where $u_{i,j}$ represents the velocity gradient tensor, $\|\Omega_{i,j}\|^2 = tr(\Omega_{i,j}{\Omega_{i,j}}^t)$ and $\|S_{i,j}\|^2 = tr(S_{i,j}{S_{i,j}}^t)$ with tr signifying the trace of a matrix. $\Omega_{i,j}$ and $S_{i,j}$ denote the local vorticity tensor and strain rate tensor, which mathematically are given by

$$\Omega_{i,j} = \frac{1}{2}(u_{i,j} - u_{i,j}) \text{ and} \tag{3.7}$$

$$S_{i,j} = \frac{1}{2}(u_{i,j} + u_{i,j}). \tag{3.8}$$

In Figure 3.5, small-scale vortical structures are clearly captured in the near-wall regions. Many structures are similar to the classical hairpin structures. Generation of new hairpin structures, i.e. hairpin packets, are observed as well. These are expected typical flow features which are widely visualized and well documented in the literature pertaining to the turbulent boundary layer. However, complete prototypical hairpin structures are not very clear. This may be due to the low Reynolds number and comparatively coarse grid spacing in proximity to the wall.

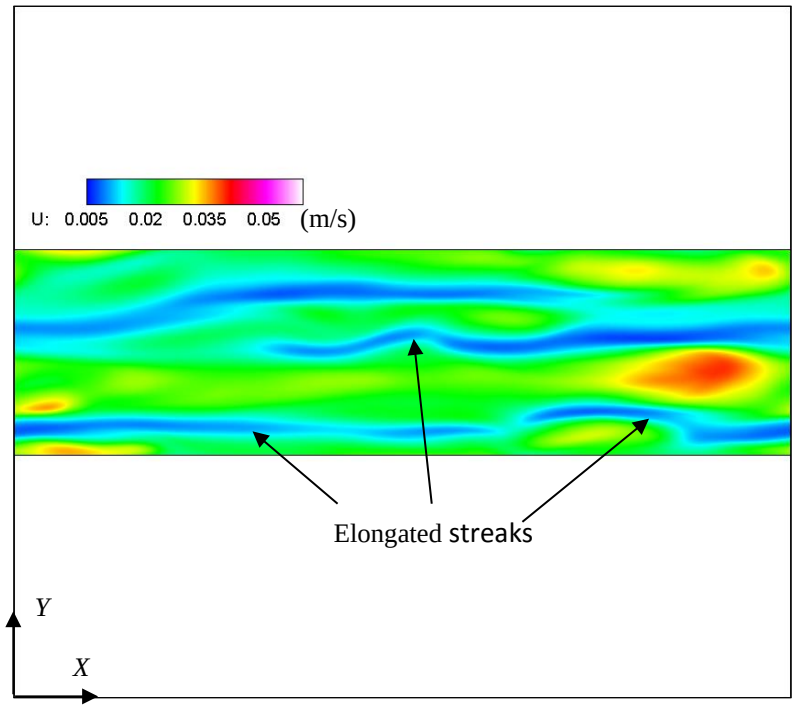

Figure 3.3. Streamwise velocity at *X*-*Y* plane (z^+ = 8.5)

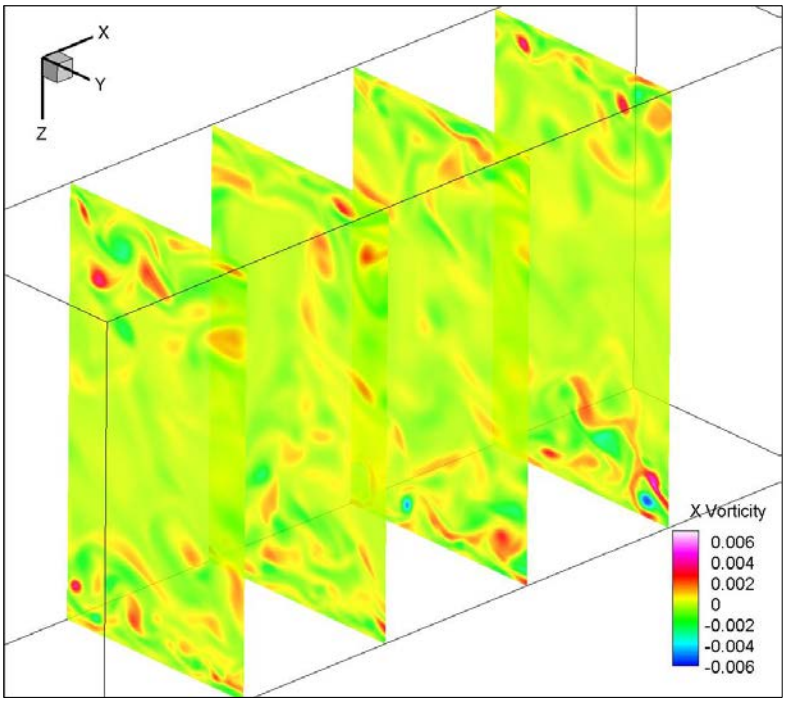

Figure 3.4. Instantaneous *X* vorticity in transverse planes

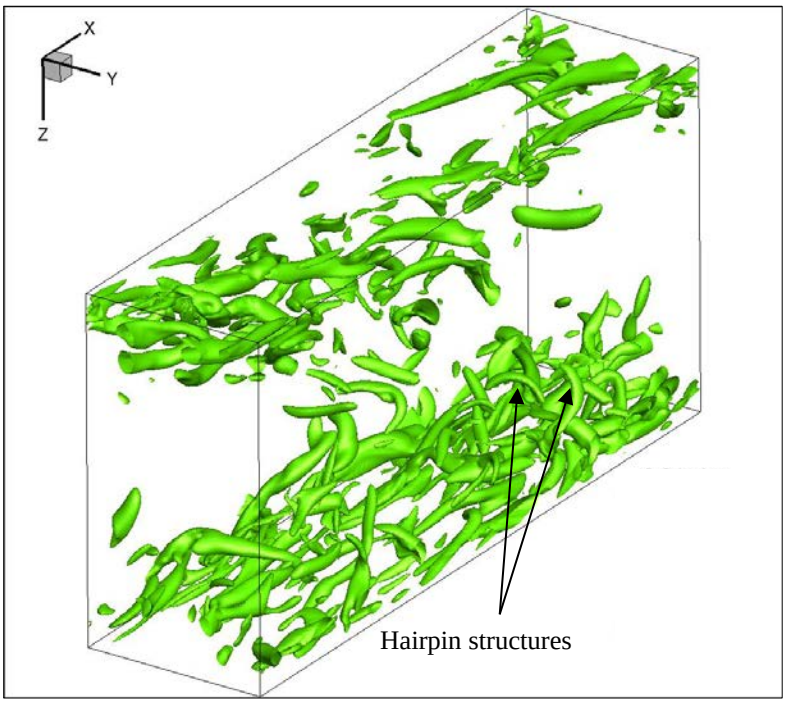

Figure 3.5. Isosurface of vortex structures near the walls (Q = 1.5E-6)

CHAPTER 4 LBM LES OF WAKE FLOW

4.1 Background

Although LBM LES is being increasingly used for simulation of fluid flow, it has not yet been widely applied to complex wake flows. Therefore, this thesis also intends to explore the capability of LBM LES in predicting a complex wake flow. In the current study, two wall-mounted cubic prisms were arranged in tandem on the bottom wall of a fully developed turbulent channel flow for a Reynolds number of $Re_H \approx 3350$ (based on the bulk velocity, U_m, and the prism height, H). This type of flow essentially provides understanding of local heat transfer and demonstrates rich flow features. Many of those flow features are sensitive to the gap spacing and the Reynolds number, which are comprehensively summarised in Martinuzzi and Havel (2000).

One major objective of the present study is to investigate the typical flow patterns around the cubic prisms and vortex structures in the wake region. Although the flow geometry is symmetric, the wake interaction introduces asymmetric behavior into the instantaneous flow. Havel (1999) and Martinuzzi and Havel (2000) investigated a thin boundary layer over two wall-mounted cubes in tandem experimentally as a function of the inter-obstacle spacing, S_{gap}, at $Re_H = 22{,}000$. Three distinct flow regimes were identified based on the vortex shedding behavior in the wake of the cubes in their studies. For a small gap, i.e. $S_{gap}/H < 1.4$, the shear layer separates at the front edges of the leading cube and reattaches on the sides of the downstream cube, yielding two intermittent oscillations behind the second cube (Havel 1999). A medium gap, i. e. $1.4 < S_{gap}/H < 3.5$, is characterised by a constant value of the Strouhal number ($St = f\, S_{gap}/U_B$, where f is the shedding frequency and U_B is the bulk velocity) (Martinuzzi and Havel 2000). For a large gap, i.e. $S_{gap}/H > 4$, a second horse-shoe vortex is observed in front of the downstream cube. The dominant frequency in the wake downstream of the second cube is close to that of the single cube case, and thus independent of the gap distance (Havel 1999).

Meinders and Hanjalić (1999) experimentally explored a similar type of flow over a cube within a structured array at a relatively low Reynolds number of $Re_H = 3854$ based on the bulk velocity. The array of cubes used an in-line matrix with an uniform inter-obstacle spacing of

$S_{gap} = 3H$. The typical flow features and mean flow patterns around the cube, i.e. vortex structure and reattachment of separated shear layer, *etc.*, were reported along with a Strouhal number of *St* = 0.109 in the wake region. Meinders and Hanjalić (2002) reported an experimental investigation of two-wall mounted cubes. Both tandem and staggered patterns were considered with various gap distances over a wide range of Re_H values. A proto-typical horseshoe vortex was visualized in front of the upstream cube due to the adverse pressure gradient. Shear flow separated from the top leading edge of the upstream cube intruded into the gap forming a recirculation vortex. Flow separation at the leading edges also gave rise to the vortices. The local heat transfer and other flow features were well documented in their study as well. The current simulation reproduces the experiment by Meinders and Hanjalić (2002) for a Reynolds number of $Re_H = 3900$ using an inter-obstacle spacing of $S_{gap} = H$.

This chapter is organized as follows. The formulation of the standard Smagorinsky SGS model will first be reviewed in Section 4.2, followed by the details of the computational specification in Section 4.3. This chapter then proceeds with an analysis of the flow in Section 4.4, 4.5 and 4.6 from three perspectives: mean flow patterns, instantaneous flow features and Proper Orthogonal Decomposition (POD), respectively.

4.2 Standard Smagorinsky SGS model

A standard Smagorinsky SGS model is used for the current LES to capture the subgrid-scale motions. The eddy viscosity employed in the model is in fact obtained based on the assumption that the energy production is balanced by the dissipation (Germano *et al*. 1991). Therefore, the SGS viscosity is given by (Yu 2004)

$$\nu_{SGS} = (C_s \Delta_x)^2 \bar{S}, \tag{4.1}$$

where $C_s = 0.1$, Δ_x is the reference length scale given by $\Delta_x = \delta_x$, and $\bar{S} = \sqrt{2S_{i,j}S_{i,j}}$. The strain rate tensor, $S_{i,j}$, is calculated using the local velocity field based on the finite difference relations (Hossain *et al.* 2015). The total viscosity is then obtained by the summation of the SGS viscosity and molecular viscosity. The corresponding relaxation parameters, S_9 and S_{13}, become

$$S_9 = S_{13} = \frac{1}{3(\nu_{SGS} + \nu_0) + 0.5}. \tag{4.2}$$

In the regions near the walls and the cubic prisms, the van Driest damping function is used to capture reduction in the turbulence length scale (Hossain *et al.* 2015), i.e.

$$\Delta_x = \delta_x \left[1 - \exp\left(-\frac{z^+}{A}\right)\right], \tag{4.3}$$

where $z^+ = zu_\tau/\nu_0$ is the normalized distance measured from the walls in the vertical direction and the cubes in directions normal to the surfaces. $u_\tau = \sqrt{\tau_w/\rho}$ is the local friction velocity with τ_w signifying the wall shear stress, and the value of the coefficient is A = 25. The magnitude distribution of the SGS viscosity in the domain will be depicted in Section 4.5 below.

4.3 Computational specifications

The computational domain of the current study was discretized uniformly using a grid of 325 × 112 × 182 in the streamwise (X), spanwise (Y) and wall-normal (Z) directions, respectively. Two cubic prisms were mounted on the bottom wall of the channel with a gap distance of $S_{gap}/H = 1$. Each of the prisms was represented by a set of 36 × 36 × 36 gridpoints. The height of the prism in wall units was $z^+ = 175$, which was located in the overlap region. When normalized using the prism height, shown in Figure 4.1, the computational domain extended 9H × 3.2H × 5H in the X, Y, and Z directions, respectively. The upstream cube was located a distance of 1.5H away from the inlet plane. Based on the frontal area of the cubic prism and cross-section area of the solution domain, the blockage ratio was 6.36%. A spanwise distance of 3.2H only provides a minimum width for the wake flow in the current study and would be inappropriate for a flow with a wide wake region.

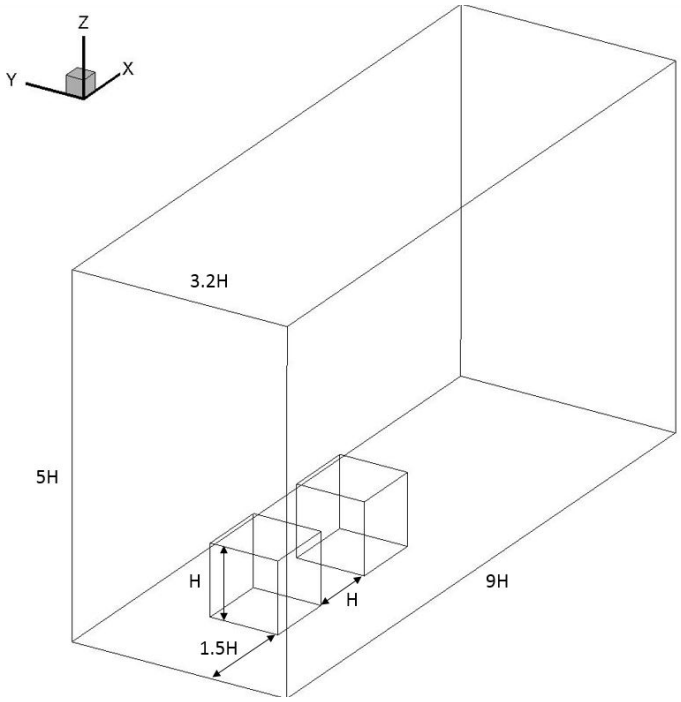

Figure 4.1. Computational domain

A Reynolds number of $Re_H \approx 3350$ based on the bulk velocity and prism height was used in the current simulation. The inlet boundary condition was implemented via a pre-cursor turbulent channel inflow. Its domain was defined by $3.5H \times 3.2H \times 5H$, and can be visualized as being upstream of the target domain. Note that the streamwise distance of the upstream domain may not be sufficiently long to yield a statistically accurate profile, but it is sufficient to provide an adequate inlet condition for the target domain though. An external force representing the effect of a pressure gradient served to drive the pre-cursor flow. At each time step, the velocity profile of an upstream fully developed turbulent channel flow was extracted and prescribed as an inlet velocity profile for the flow over the cubic prisms in the downstream target domain (Koda 2013). The instantaneous vortex structure in the upstream domain is presented below in Figure 4.2 where typical hairpin structures are observed.

The configuration used in current study is schematically depicted in Figure 4.3 where the instantaneous velocities at the indicated planes are identical for each time step, i.e. $\overrightarrow{U_\alpha}(u, v, w) = \overrightarrow{U_\beta}(u, v, w)$. For the downstream domain, a constant pressure was specified at the outlet. A halfway

bounce-back scheme was utilized to achieve the no-slip boundary conditions at the solid walls and a periodic boundary condition was applied in the spanwise direction. Details associated with the boundary conditions are specified in Section 2.4.

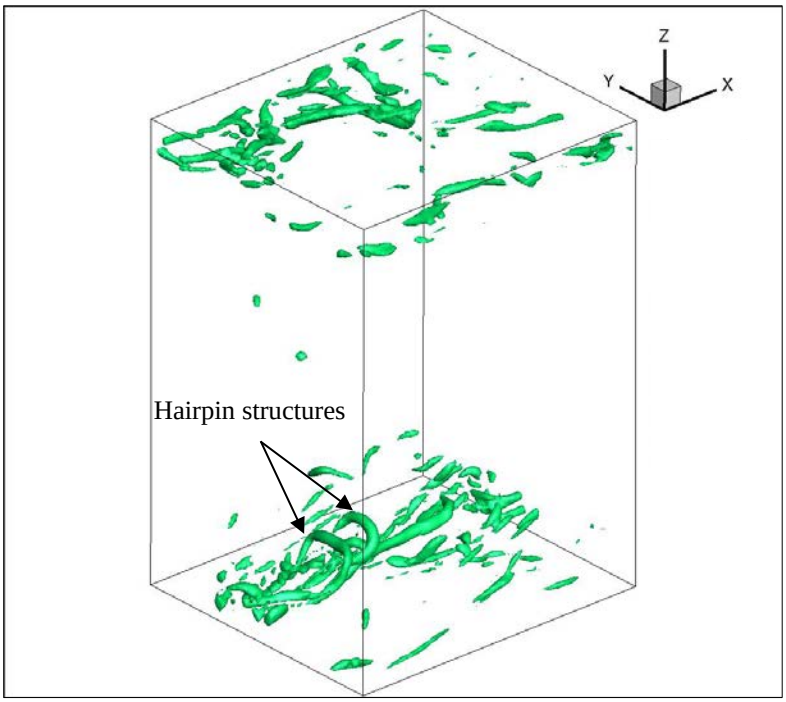

Figure 4.2. Isosurface of vortex structures in precursor turbulent inflow (Q = 1.25)

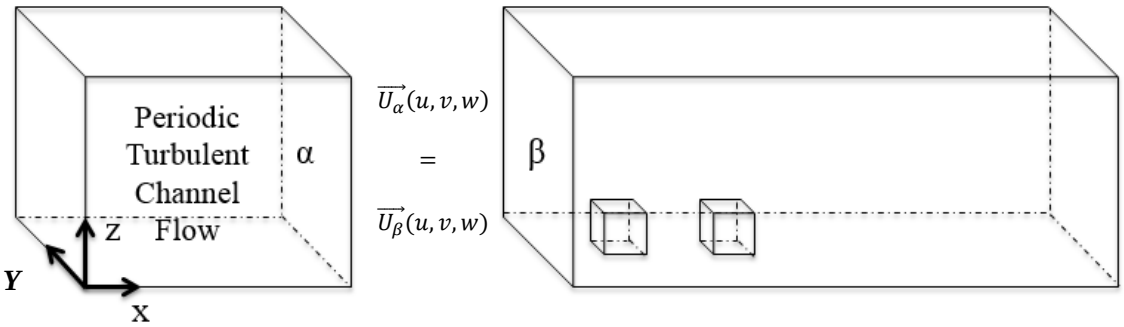

Figure 4.3. Schematic of specification of inflow using precursor channel flow.

4.4 Mean flow patterns

Figure 4.4(a) presents the mean flow pattern in a horizontal plane located at the mid-height of the cubes. The mean flow is symmetric. Recirculation regions are observed along the lateral sides of the upstream cube, and present both in the gap and behind the downstream cube. The corresponding center locations of the recirculation zones, summarized in Table 4.1, reasonably match those observed by Meinders and Hanjalić (2002) for $Re_H \approx 3900$. Note that the measurements were performed with the origin located at the intersection point of the leading edge of the upstream cube and centerline of the channel in Figure 4.4(a). In the vertical mid-plane (*X*-*Z*) shown in Figure 4.4(b), a horseshoe vortex and a recirculation region are identified in front of and on the top surface of the upstream cube, respectively. The flow splits at the leading edge of the downstream cube, forming a boundary layer along its top surface and a strong recirculation region in the gap. Recirculation is also evident behind the downstream cube.

Table 4.1. Locations of centers of recirculation zones

	$X/H, Y/H$ **Current LES**	$X/H, Y/H$ **Meinders and Hanjalić (2002)**
Recirculation along sides	0.58, 0.63	0.57, 0.63
Recirculation in the gap	1.43, 0.42	1.41, 0.43
Recirculation in the wake	3.61, 0.31	3.55, 0.30

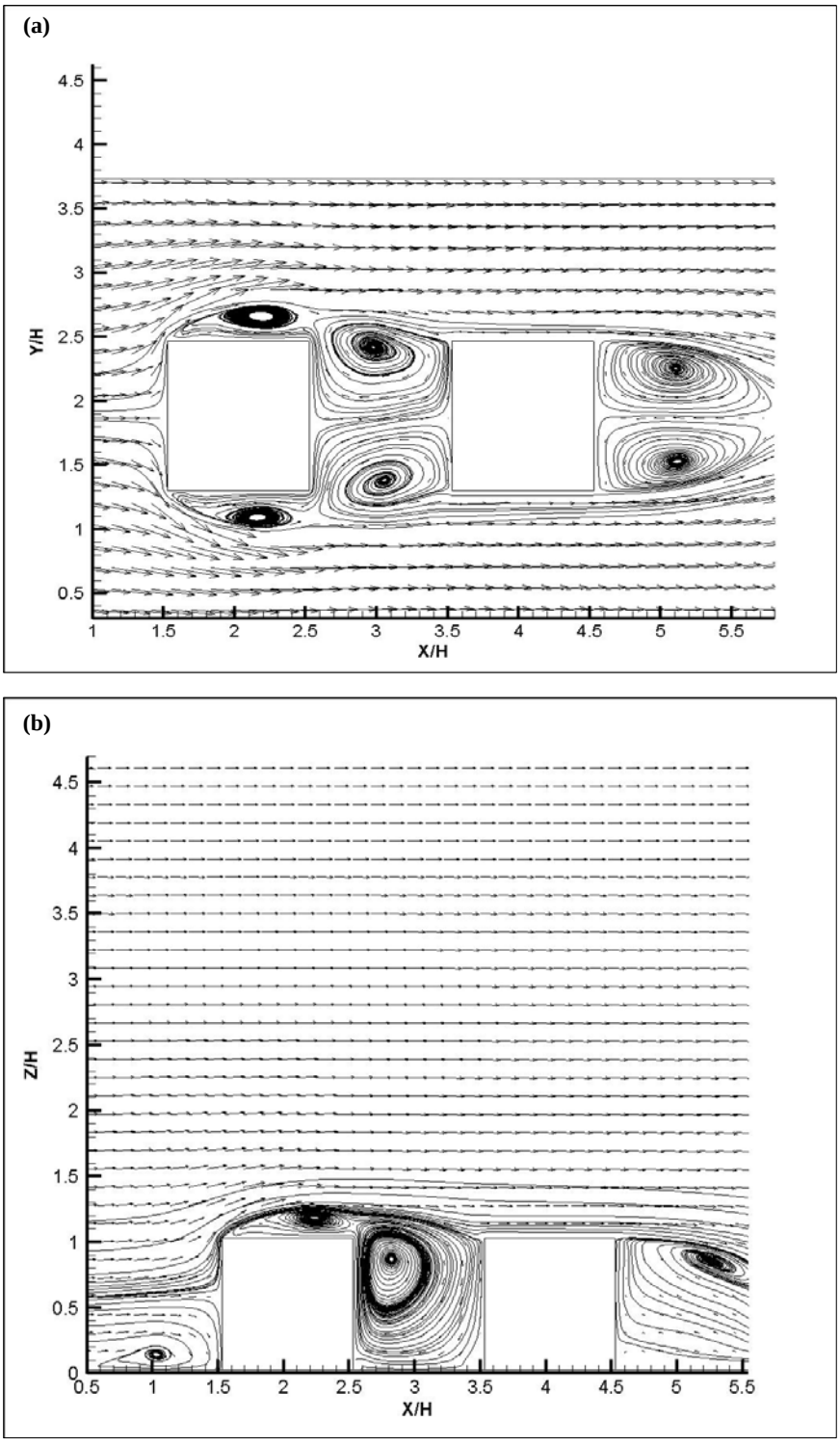

Figure 4.4. (a) Streamline and vectors of mean velocity in an enlarged *X*-*Y* plane (Z/*H* = 0.5); (b) Streamline and vectors of mean velocity in an enlarged *X*-*Z* plane (vectors are plotted at every 2nd node)

4.5 Instantaneous flow features

Figure 4.5 demonstrates the instantaneous *Y* vorticity in the vertical mid-plane of the channel, and *Z* vorticity in the horizontal mid-plane of the cubes. In the vertical plane, a horseshoe vortex is observed in front of the upstream cube. Separated shear flow from the leading edge of the upstream cube reattaches back onto the top surface. The impinging flow splits at the leading edge of the downstream cube. Part of the flow forms a recirculation region in the gap and the remainder develops into a boundary layer on the top surface of the downstream cube. In the wake region, the separated shear layers interact with one another intensely, forming complex vortices extending far down stream. These instantaneous features are also reflected in the horizontal plane, although the vorticity magnitude is different.

Figure 4.6 depicts the SGS viscosity normalized by the molecular viscosity. Typical flow features observed in Figure 4.5 are also reflected here in this figure where $\nu_{SGS}/\nu_0 = 0.35$ is plotted. In the regions near the cubic prisms, ν_{SGS} is much higher than elsewhere.

Figure 4.7 presents the instantaneous vortex structures visualized using the *Q* criterion. The vortex structures around the cubes present a high degree of intensity and complexity. The separated shear layers from the cubes extend far downstream while interacting with one another and with the surrounding shear flow. A closer look at the vortex structures reveals two horseshoe vortices in front of the upstream cube; the one closer to the cube is more persistent and intrudes into the gap region, thus resulting in instantaneous asymmetric flow patterns. Separated shear layers from the leading edges of the upstream cube trigger the development of the vortex field. Some vortex structures around the cubes appear to resemble proto-typical hairpin structures.

Figure 4.8 demonstrates the instantaneous fluid structures in the gap region between the two cubic prims. The intrusion of the separated shear flows from the upstream observed in Figure 4.7 is also evident in Figure 4.8(a) where small streamwise tubes are observed entering the gap region from its top and lateral sides. Meanwhile, close to the end of the gap region shown in Figure 4.8(b), small, but fairly strong, vortices present a higher level of intensity than any other location between the cubes.

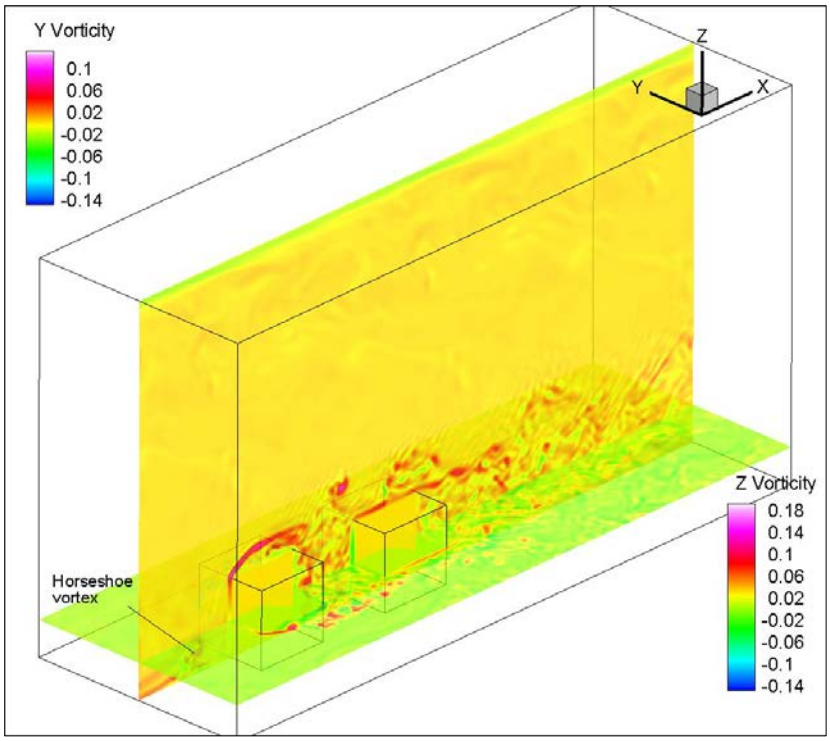

Figure 4.5. Instantaneous vorticity in mid-height plane and vertical mid-plane

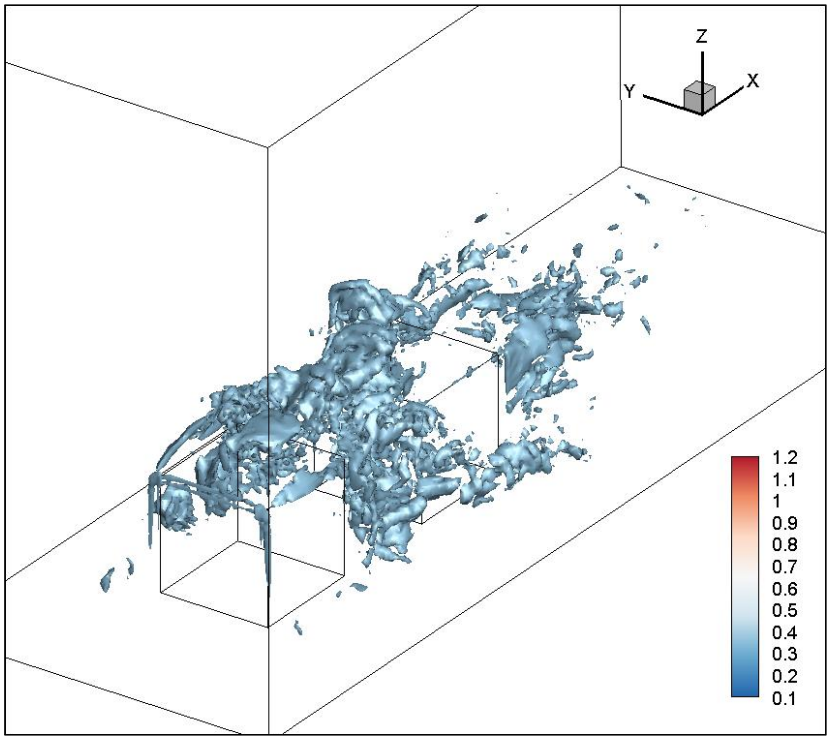

Figure 4.6. Instantaneous normalized SGS viscosity (ν_{SGS}/ν_0 = 0.35)

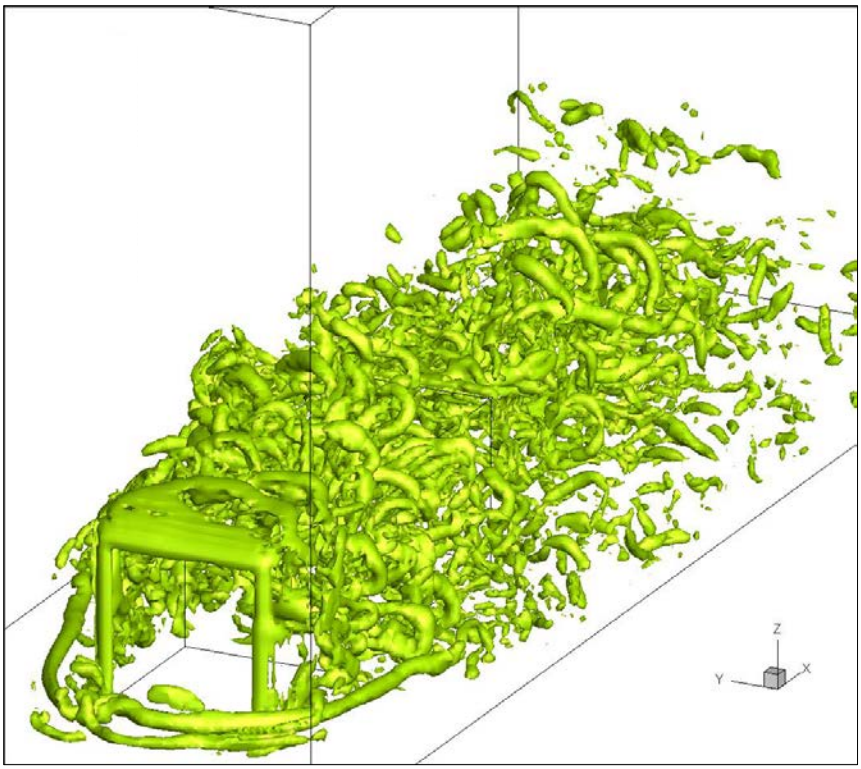

Figure 4.7. Visualization of instantaneous vortex structures using Q criterion (Q = 28)

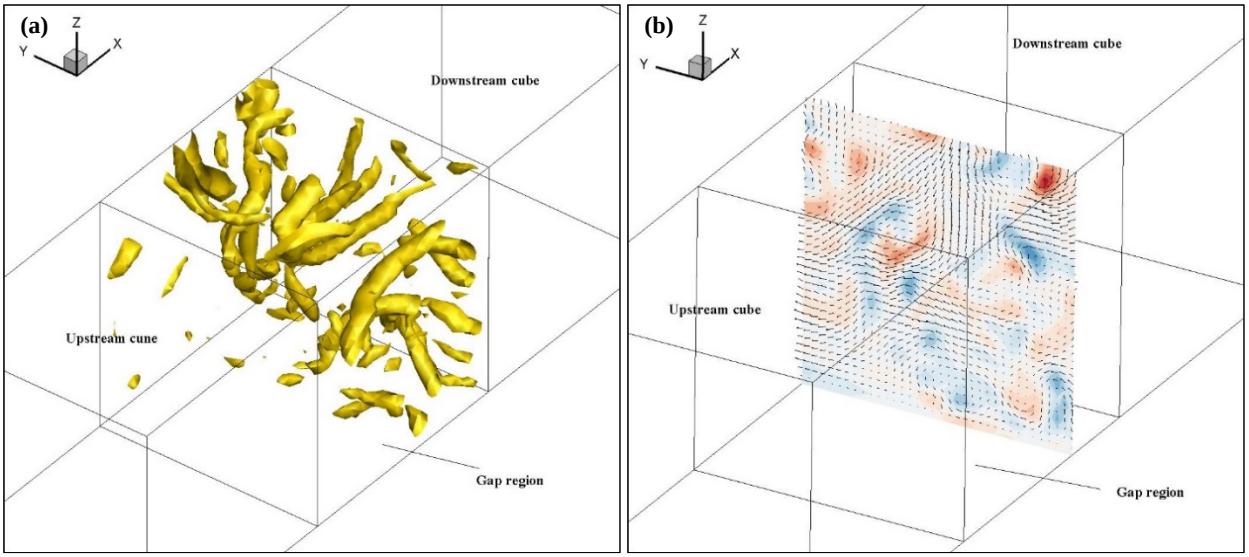

Figure 4.8. (a) Instantaneous vortex structures in the gap region; (b) Instantaneous X vorticity in transverse plane.

4.6 Proper orthogonal decomposition

An investigation was performed via a three-dimensional Proper Orthogonal Decomposition (POD) in the gap region located between the cubic prisms where the flow structures demonstrated a fairly high complexity. POD was initially employed for identifying the dynamic coherent structures in turbulent flows (Kim *et al.* 2005). It is capable of efficiently extracting different energetic structures in a flow via a finite number of eigenmodes that capture most of the fluctuation energy (Kim *et al.* 2005, Hossain *et al.* 2015). The current investigation employs the snapshot version of POD to study the flow structures in the gap region. Originally developed by Sirovich (1987), this version of POD could be conveniently applied to both of experimental and numerical data sets.

In the current POD analysis, the empirical eigenfunctions were obtained from the LBM LES data sets, i.e. (Kim *et al.* 2005),

$$\phi_k(x, y, z, t) = \sum_{i=1}^{M} A_{ki}\, u_i'(x, y, z, t_i), \tag{4.4}$$

where ϕ_k denotes the k^{th} eigenfunction, $\boldsymbol{M}$ is the number of snapshots, and $u_i'(x, y, z, t_i)$ represents the fluctuation velocity field at the i^{th} time step. In equation 4.4, A_{ki} stands for the k^{th} eigenvector that is determined via the algebraic eigenvalue problem given by (Sirovich 1987)

$$\mathcal{C}A = \lambda A, \tag{4.5}$$

where $\mathcal{C}$ is a $\boldsymbol{M} \times \boldsymbol{M}$ square matrix solved over a target domain, ζ. It is given by

$$\mathcal{C} = \frac{1}{M} \int u_m'(x, y, z, t_i) \cdot u_n'(x, y, z, t_i) d\zeta, \tag{4.6}$$

and $u_m'(x, y, z, t_i)$ is the conjugate transpose of $u_n'(x, y, z, t_i)$. Equation 4.5 is solved for the eigenvalues, λ_k, and eigenvectors, A_k . Note that, with respect to the kinetic energy contributed by the corresponding eigenfunctions, eigenvalues are referenced in descending order with λ_1 standing for the largest value and λ_m the least (Kim *et al.* 2005).

The current POD analysis considered an interrogation area of $H \times H \times H$, covering the entire region between the cubes. A total of $\boldsymbol{M} = 200$ instantaneous snapshots was collected for every 360 time steps. Convergence was reached at approximately the 135^{th} eigenfunction of the fluctuating velocity field as shown below in Figure 4.9. Note that a total of 90% of the fluctuation energy could be captured by only 130 eigenfunctions.

Figure 4.10 demonstrates the mean flow structures in the gap region based on an average of 200 instantaneous data sets with the visualization being realized using *Q* criterion. Two large continuous structures are observed spreading along each of two lateral sides, where the separated shear flow intrudes into the gap. Close to the front face of the downstream prism, the two side structures tend to merge together at the top. This is probably because the upstream impinging flow splits at the top leading edge of the downstream cube and part of it intrudes into the gap region.

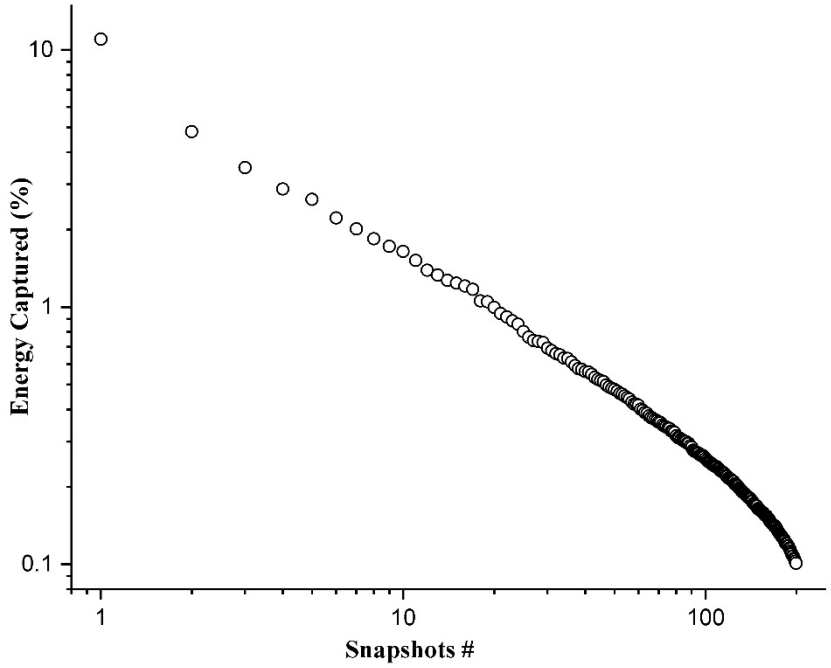

Figure 4.9. Energy captured with each eigenmode of POD

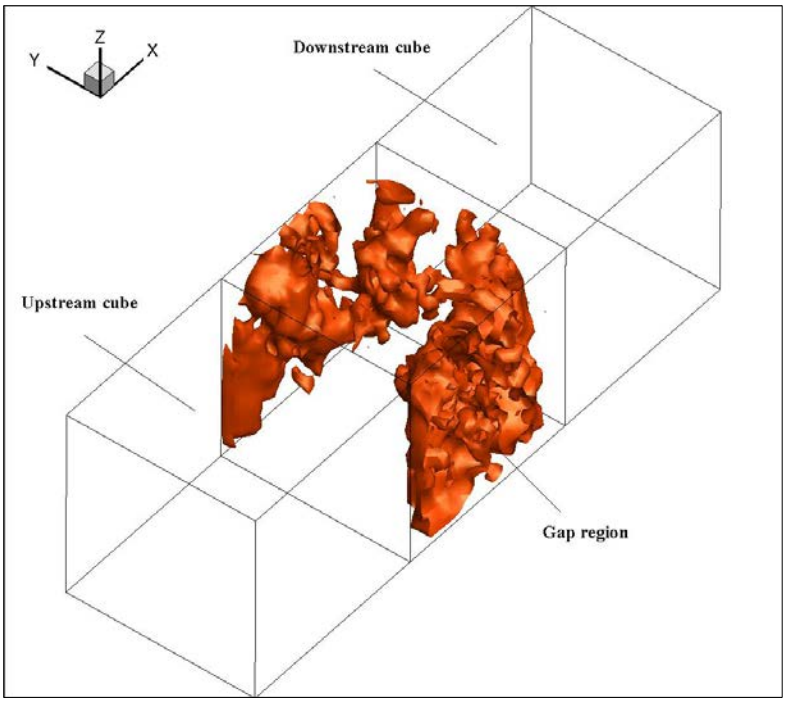

Figure 4.10. Mean flow structures of the gap region (*Q* = 1.80E-6)

Figure 4.11 presents a visualization of the flow structure based on four different eigenfunctions of the fluctuating velocity field. The selected empirical eigenfunctions were determined using equation 4.4. As shown in Figure 4.11(a) and (b), large-scale structures were captured by both of the 1st and 5th eigenfunctions contributing 11.03% and 2.63% to the total energy, respectively. A single large structure is clearly identified in front of the downstream cube in Figure 4.11(a), indicating where the intruding flows begin to merge in the gap. It also reflects the most energetic eigenmode. Smaller-scale structures are associated with the 5th eigenfunction shown in Figure 4.11(b). One fairly large structure is observed close to the upper front surface of the downstream cube along with a smaller disconnected rotational structure along the top leeward edge of the upstream cube. This may reflect the locations where the shear flow starts to intrude from the top. Figure 4.11(c) and (d) represent relatively smaller-scale structures along the sides of the gap region; these were captured by the 10th and 50th eigenfunctions, respectively, characterizing 1.65% and 0.48% of the total kinetic energy. A closer look at all four figures reveals that no dominant structures were present in the central region of the gap, and that the structures tend to

crowd together closer to the front face of downstream cube. This is also consistent with the observation in Figure 4.8.

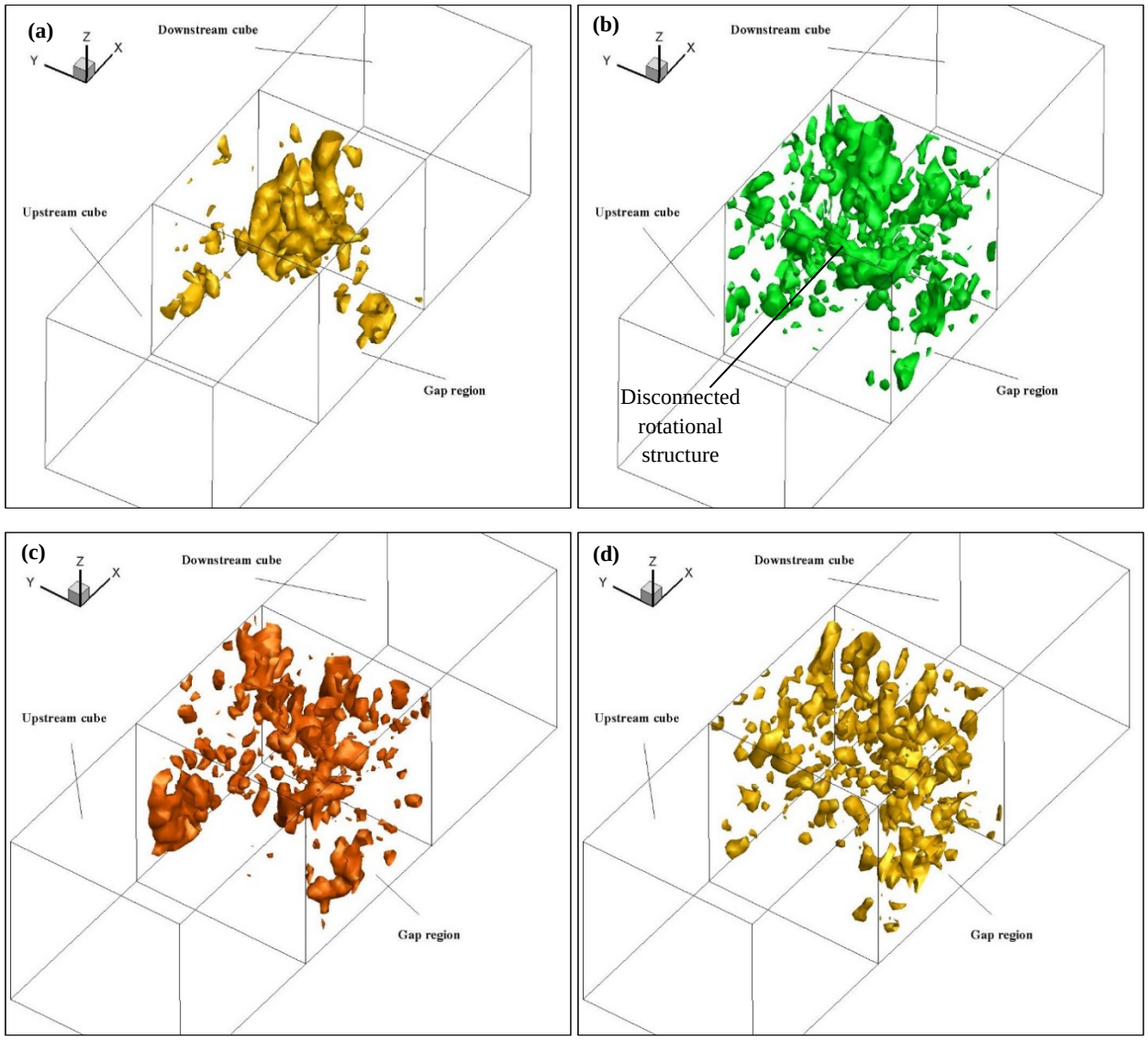

Figure 4.11. Vortex structures visualized using Q criteria: (a) 1st eigenfunction (Q = 4.50E-7); (b) 5th eigenfunction (Q = 4.50E-7); (c) 10th eigenfunction (Q = 8.50E-7); (d) 50th eigenfunction (Q = 2.50E-6)

CHAPTER 5 CONCLUSIONS AND FUTURE WORK

5.1 Conclusions

Disordered and chaotic, turbulent flow is well known for its practical importance and formidable complexity. A numerical study of turbulent flows was performed in the current research using a novel numerical approach called the lattice Boltzmann method. Widely considered to present a potential alternative to solving the Navier-Stokes equations, LBM is indeed an efficient approach in computational fluid dynamics and demonstrates two particularly attractive advantages over a traditional method: simple algorithm and parallel scalability (Koda 2013). The simplicity in algorithm originates from the fact that there is no pressure solver involved to correct the velocity field, and the parallel suitability arises from its inherent nature of streaming-collision process. The current research employed a newly developed code using the MRT LBM to study the three-dimensional turbulent flows based on a D3Q19 lattice model. Four types of boundary schemes were developed to realize a no-slip wall, periodic flow, precursor inlet flow and constant outlet pressure. The current LBM scheme simulated the effects of a pressure gradient to drive the fluid flow via a source term in the particle distribution functions. An initial flow state based on a one-seventh power law profile superimposed by three-dimensional sinusoidal perturbations was used to reduce the computational effort to trigger turbulence in the developing stage of turbulent channel flow.

One major deficiency of the LBM originates from its inherent uniformity in the computational domain. This drawback imposes a constraint over its application to complex flows. The current study attempted to solve this issue using local grid refinement. The scheme under consideration is volumetrically formulated, and thus it well preserves the laws of conservation. In addition, implementation of the current scheme is fairly straightforward because of its simple algorithm. Due to the time constraint, only a laminar channel flow of $Re \approx 1.08$ was used for a preliminary test where the regions near the walls were refined locally. The velocity profile is in excellent agreement with the analytical solution.

A validation of the developed LBM DNS was implemented by simulating a turbulent channel flow for a Reynolds number of $Re_\tau \approx 230$. The mean flow variables, velocity profiles and Reynolds stress profiles were compared to those from the literature for a Reynolds of $Re_\tau \approx 180$ (Kim *et al.* 1987). Good agreements are obtained for all comparisons, except for some slight over-predictions due to the difference in Reynolds numbers. Instantaneous vorticity visualization was realized in four *X-Z* cross-sections. Small-scale wall-induced coherent structures are clearly observed in the near wall regions as expected. The structures expand in size with increasing distance away from the wall. A second invariant criterion was employed to visualize the vortex structure. Elongated streaks are clearly identified in the near wall regions. Typical hairpin structures are not clearly evident. The reasons are believed to be the low Reynolds number and relatively coarse grid spacing in the vicinity of the wall.

The last investigation of the current research was associated with a turbulent flow over two cubic prisms placed in a channel. A Reynolds number of $Re_H \approx 3350$, based on the bulk velocity and prism height, was realized in the current simulation. The inlet boundary condition was implemented via a pre-cursor turbulent channel inflow whereas the outlet plane was maintained at a constant pressure. An LES was incorporated in the framework of LBM based on the standard Smagorinsky SGS model. For the mean flow features, a symmetric pattern is well identified in a horizontal plane located at the mid-height of the cubes. The locations of the recirculation centers are found to be reasonably consistent with those identified in literature for $Re_H \approx 3900$ (Meinders and Hanjalić 2002). In the vertical mid-plane, a horseshoe vortex is identified in front of the upstream prism along with a recirculation region observed on its top surface. The flow splits at the leading edge of the downstream cube, forming a boundary layer along its top surface and a strong recirculation region in the gap. Recirculation is also clearly evident behind the downstream cube. On the other hand, instantaneous visualizations using the second invariant criterion reveal that the vortices around the prisms shedding far downstream present a high degree of complexity and intensity. Some of these vortices resemble proto-typical hairpin structures. In the gap region, the flow structures close to the front face of downstream cube indicate a relatively higher intensity. A snapshot version of POD analysis was implemented in the gap region. This technique is in effect capable of presenting different energetic structures in a flow via a finite number of eigenfunctions. Visualized using Q criterion, flow structures come in different sizes and locations with various eigenfunctions signifying different energy distributions. It is revealed that the highest energy

structures are identified in front of the downstream cube where the intruding flows actually start to merge in the gap. Meanwhile, structures also tend to crowd together closer to the front face of downstream cube.

5.2 Future work

A newly developed LBM code in the current study demonstrates a fairly good performance in capturing the fluid features both of the wall-bounded turbulent flow and the flow field involving some geometric complexity. Further improvements in its predictive capability and computational efficiency could include, but not be limited to, the following perspectives:

- **Parallel computing**

  Parallel scalability of the LBM is one of its key advantages over the traditional approach. With parallelization, computational efficiency will be considerably increased.

- **Lattice model with more velocity sites**

  Although more velocity sites in the lattice model will inevitably increase the complexity in algorithm, it is necessary for the flow field involving more complex geometries. To increase the capability of the current MRT LBM, D3Q27 will be a good option.

- **Boundary conditions**

  A halfway bounce-back scheme is sufficient to realize the no-slip boundary condition along a plane. However, it only demonstrates first-order accuracy for curved surfaces. A more effective boundary condition, such as the immersed boundary scheme, is therefore necessary in order to effectively handle the challenges arising from the complex geometries.

- **Dynamic subgrid scale model**

  One major drawback of the standard Smagorinsky SGS model lies in its inability to accurately predict the flow features in some complex turbulent fields due to the constant model coefficient (Germano *et al.* 1991). This disadvantage could be eliminated by implementing a dynamic SGS model.

- **Local grid refinement**

  One preliminary test of the local grid refinement using laminar channel flow is far from being sufficient for judging its proficiency. A turbulent channel flow would be necessary for the next step to further test its capability. Meanwhile, it was reported that unphysical discontinuities were observed in the higher-order turbulence statistics profiles (Premnath *et al.* 2009a) using a similar approach. Hence, a further study to improve this deficiency is required.

REFERENCES

Bespalko, D. J. 2006. "Direct numerical simulation of turbulent channel flow using the lattice Boltzmann method." M.Sc. Thesis, Department of Mehanical and Materials Engineering, Queen's University, Kingston, ON, Canada

Chen, H., O. Filippova, J. Hoch, K. Molvig, R. Shock, C. Teixeira, and R. Zhang. 2006. "Grid refinement in Lattice Boltzmann methods based on volumetric formulation." *Physica A* 362: 158-167.

Chikatamarla, S. S., C. E. Frouzakis, I. V. Karlin, A. G. Tomboulides, and K. B. Boulouchos. 2010. "Lattice Boltzmann method for direct numerical simulation of turbulent flows." *Journal of Fluid Mechanics* 656: 298-308.

Dean, R. B. 1978. "Reynolds number dependence of skin friction and other bulk flow variables in two-dimensional rectangular duct flow. "*Transactions of the ASME: Journal of Fluids Engineering* 100(2): 215.

D'Humieres, D., I. Ginzburg, M. Krafczyk, P. Lallemand, and L. Luo. 2002. "Multiple-relaxation-time lattice Boltzmann models in three dimensions." *Philosophical Transactions: Mathematical, Physical and Engineering Sciences* 360: 437-451.

Dupuis, A., and B. Chopard. 2003. "Theory and applications of an alternative lattice Boltzmann grid refinement algorithm." *Physical Review E* 67: 066707.

Eitel-Amor, A., M. Meinke, and W. Schröder. 2013. "A lattice-Boltzmann method with hierarchically refined meshes." *Computers & Fluids* 75: 127-137.

Filippova, O., and D. Hanel. 1998. "Grid refinement for lattice-BGK models." *Journal of Computational Physics* 147 (1): 219-228.

Freitas, R. K., A. Henze, M. Meinke, and W. Schröder. 2011. "Analysis of lattice-Boltzmann methods for internal flows." *Computers & Fluids* 47: 115-121.

Freitas, R. K., M. Meinke, and W. Schroder. 2006. "Turbulence simulation via the lattice-Boltzmann method on hierarchically refined meshes." *European Conference on Computational Fluid Dynamics.* The Hague, Netherlands. 1-12.

Germano, M., U. Piomelli, P. Moin, and W. H. Cabot. 1991. "A dynamic subgrid-scale eddy viscosity model." *Physics of Fluids* A3 (7): 1760-1765.

Havel, B. 1999. "Experimental investigation of turbulent flow generated by two interfering surface-mounted cubes in a thin boundary layer." M.Sc. Thesis, Department of Mechanical and Materials Engineering, The University of Western Ontario, London.

He, X., and L. Luo. 1997. "A priori derivation of the lattice Boltzmann equation." *Physical Review E* 55: R6333–6.

He, X., L. Luo, and M. Dembo. 1996. "Some progress in lattice Boltzmann method. Part I. Nonuniform mesh grids." *Journal of Computational Physics* 129: 357-363.

He, X., Q. Zou, L. Luo, and M. Dembo. 1997. "Analytic solutions of simple flows and analysis of nonslip boundary conditions for the lattice Boltzmann BGK model." *Journal of Statistical Physics* 87: 115-136.

Hossain, S., D. J. Bergstrom, and X. B. Chen. 2015. "Visualisation and analysis of large-scale vortex structures in three-dimensional turbulent lid-driven cavity flow." *Journal of Turbulence* 16: 901-924.

Hou, S, J. Sterling, S. Chen, and G. D. Doolen. 1996. "A lattice Boltzmann subgrid model for high Reynolds number flows." *arXiv:comp-gas/9401004* 6: 151-166.

Hunt, J.C.R., A. A. Wary, and P. Moin. 1988. "Eddies, streams and convergence zones in turbulent flows." *Center for Turbulence Research Proceedings of the Summer Program.* 193-208.

Jafari, S., M. Rahnama, and E. J. Javaran. 2014. "Simulation of turbulent duct flow by employing shear-improved Smagorinsky model accompanied by forced generalized lattice Boltzmann method." *International Journal of Numerical Methods for Heat & Fluid Flow* 24: 86-102.

Jeong, J., and F. Hussain. 1995. "On the identification of a vortex." *Journal of Fluid Mechanics* 285: 69-94.

Kim, J., P. Moin, and R. Moser. 1987. "Turbulence statistics in fully developed channel flow at low Reynolds number." *Journal of Fluid Mechanics* 177: 133-166.

Kim, Y., D. Rockwell, and A. Liakopoulos. 2005. "Vortex buffeting of aircraft tail: interpretation via Proper Orthogonal Decomposition." *AIAA Journal* 43 (3): 550-559.

Koda, Y. 2013. "Lattice Boltzmann method for simulating turbulent flows." M.Sc. Thesis, Department of Mechanical Engineering, University of Waterloo, Waterloo, ON, Canada

Kuwata, Y., and K. Suga. 2016. "Imbalance-correction grid-refinement method for lattice Boltzmann flow simulations." *Journal of Computational Physics* 311: 348-362.

Lam, K. L. 1989. "Numerical investigation of turbulent flow bounded by a wall and a free-slip surface." PhD Thesis, Department of Chemical Engineering, University of California, Santa Barbara, Santa Barbara, CA, USA.

Martinuzzi, R. J., and B. Havel. 2000. "Turbulent flow around two interfering surface-mounted cubic obstacles in tandem arrangment." *Transactions of the ASME: Journal of Fluids Engineering* 122: 24-31.

Meinders, E. R., and K. Hanjalic. 2002. "Experimental study of the convective heat transfer from in-line and staggered configurations of two wall-mounted cubes." *International Journal of Heat and Mass Transfer* 45: 465-482.

Meinders, E. R., and K. Hanjalic. 1999. "Vortex structure and heat transfer in turbulent flow over a wall-mounted matrix of cubes." *International Journal of Heat and Fluid Flow* 20: 255-267.

Mussa, A., P. Asinari, and L. Luo. 2009. "Lattice Boltzmann simulations of 2D laminar flows past two tandem cylinders." *Journal of Computational Physics* 228: 983-999.

Premnath, K. N., M. J. Pattison, and S. Banerjee. 2013b. "An investigation of the lattice Boltzmann method for large eddy simulation of complex turbulent separated flow." *Transactions of the ASME: Journal of Fluids Engineering* 135: 1-12.

Premnath, K. N., M. J. Pattison, and S. Banerjee. 2013a. "Computation of transitional flow past a circular cylinder using multiblock lattice Boltzmann method with a dynamic subgrid scale model." *Fluid Dynamics Research* 45: 1-26.

Premnath, K. N., M. J. Pattison, and S. Banerjee. 2009a. "Generalized lattice Boltzmann equation with forcing term for computation of wall-bounded turbulent flows." *Physical Review E* (79): 1-19.

Premnath, K. N., Martin J. P., and Sanjoy B. 2009b. "Dynamic subgrid scale modeling of turbulent flows using lattice-Boltzmann method." *Physica A* 388 (13): 2640-2658.

Rohde, M., D. Kandhai, J. J. Derksen, and K.E.A. van den Akker. 2006. "A generic, mass conservative local grid refinement technique for Lattice-Boltzmann schemes." *International Journal for Numerical Methods in Fluids* 51: 439-468.

Sirovich, L. 1987. "Turbulence and dynamics of coherent structures: I-III." *Quarterly of Applied Mathematics* 45 (3): 561-590.

Staubach, D. 2013. "Static block-structured grid refinement for parallel lattice Boltzmann simulations." M.Sc. Thesis, University of Erlangen-Nuremberg, Erlangen, Germany

Versteeg, H., and W. Malalasekra. 2007. *An Introduction to Computational Fluid Dynamics.* 2nd Edition. Noida: Pearson.

Yu, H. 2004. "Lattice Boltzmann equation simulations of turbulence, mixing, and combustion." Ph.D. Thesis, Aerospace Engineering, Texas A&M University, TX, USA.

APPENDIX

The transformation matrix and its transpose are given below (Bespalko 2006):

$$M = \begin{bmatrix}
1 & 1 & 1 & 1 & 1 & 1 & 1 & 1 & 1 & 1 & 1 & 1 & 1 & 1 & 1 & 1 & 1 & 1 & 1 & 1 \\
-30 & -11 & -11 & -11 & -11 & -11 & -11 & 8 & 8 & 8 & 8 & 8 & 8 & 8 & 8 & 8 & 8 & 8 & 8 & 8 \\
12 & -4 & -4 & -4 & -4 & -4 & -4 & 1 & 1 & 1 & 1 & 1 & 1 & 1 & 1 & 1 & 1 & 1 & 1 & 1 \\
0 & 1 & -1 & 0 & 0 & 0 & 0 & 1 & -1 & 1 & -1 & 1 & -1 & 1 & -1 & 0 & 0 & 0 & 0 & 0 \\
0 & -4 & 4 & 0 & 0 & 0 & 0 & 1 & -1 & 1 & -1 & 1 & -1 & 1 & -1 & 0 & 0 & 0 & 0 & 0 \\
0 & 0 & 0 & 1 & -1 & 0 & 0 & 1 & 1 & -1 & -1 & 0 & 0 & 0 & 0 & 1 & -1 & 1 & -1 & 0 \\
0 & 0 & 0 & -4 & 4 & 0 & 0 & 1 & 1 & -1 & -1 & 0 & 0 & 0 & 0 & 1 & -1 & 1 & -1 & 0 \\
0 & 0 & 0 & 0 & 0 & 1 & -1 & 0 & 0 & 0 & 0 & 1 & 1 & -1 & -1 & 1 & 1 & -1 & -1 & 0 \\
0 & 0 & 0 & 0 & 0 & -4 & 4 & 0 & 0 & 0 & 0 & 1 & 1 & -1 & -1 & 1 & 1 & -1 & -1 & 0 \\
0 & 2 & 2 & -1 & -1 & -1 & -1 & 1 & 1 & 1 & 1 & 1 & 1 & 1 & 1 & -2 & -2 & -2 & -2 & 0 \\
0 & -4 & -4 & 2 & 2 & 2 & 2 & 1 & 1 & 1 & 1 & 1 & 1 & 1 & 1 & -2 & -2 & -2 & -2 & 0 \\
0 & 0 & 0 & 1 & 1 & -1 & -1 & 1 & 1 & 1 & 1 & -1 & -1 & -1 & -1 & 0 & 0 & 0 & 0 & 0 \\
0 & 0 & 0 & -2 & -2 & 2 & 2 & 1 & 1 & 1 & 1 & -1 & -1 & -1 & -1 & 0 & 0 & 0 & 0 & 0 \\
0 & 0 & 0 & 0 & 0 & 0 & 0 & 1 & -1 & -1 & 1 & 0 & 0 & 0 & 0 & 0 & 0 & 0 & 0 & 0 \\
0 & 0 & 0 & 0 & 0 & 0 & 0 & 0 & 0 & 0 & 0 & 0 & 0 & 0 & 0 & 1 & -1 & -1 & 1 & 0 \\
0 & 0 & 0 & 0 & 0 & 0 & 0 & 0 & 0 & 0 & 0 & 1 & -1 & -1 & 1 & 0 & 0 & 0 & 0 & 0 \\
0 & 0 & 0 & 0 & 0 & 0 & 0 & 1 & -1 & 1 & -1 & -1 & 1 & -1 & 1 & 0 & 0 & 0 & 0 & 0 \\
0 & 0 & 0 & 0 & 0 & 0 & 0 & -1 & -1 & 1 & 1 & 0 & 0 & 0 & 0 & 1 & -1 & 1 & -1 & 0 \\
0 & 0 & 0 & 0 & 0 & 0 & 0 & 0 & 0 & 0 & 0 & 1 & 1 & -1 & -1 & -1 & -1 & 1 & 1 & 0
\end{bmatrix}$$

$$M^{-1} = \begin{bmatrix}
\frac{1}{19} & -\frac{5}{399} & \frac{1}{21} & 0 & 0 & 0 & 0 & 0 & 0 & 0 & 0 & 0 & 0 & 0 & 0 & 0 & 0 & 0 & 0 & 0 \\
\frac{1}{19} & -\frac{11}{2394} & -\frac{1}{63} & \frac{1}{10} & -\frac{1}{10} & 0 & 0 & 0 & 0 & \frac{1}{18} & -\frac{1}{18} & 0 & 0 & 0 & 0 & 0 & 0 & 0 & 0 & 0 \\
\frac{1}{19} & -\frac{11}{2394} & -\frac{1}{63} & -\frac{1}{10} & \frac{1}{10} & 0 & 0 & 0 & 0 & \frac{1}{18} & -\frac{1}{18} & 0 & 0 & 0 & 0 & 0 & 0 & 0 & 0 & 0 \\
\frac{1}{19} & -\frac{11}{2394} & -\frac{1}{63} & 0 & 0 & \frac{1}{10} & -\frac{1}{10} & 0 & 0 & -\frac{1}{36} & \frac{1}{36} & \frac{1}{12} & -\frac{1}{12} & 0 & 0 & 0 & 0 & 0 & 0 & 0 \\
\frac{1}{19} & -\frac{11}{2394} & -\frac{1}{63} & 0 & 0 & -\frac{1}{10} & \frac{1}{10} & 0 & 0 & -\frac{1}{36} & \frac{1}{36} & \frac{1}{12} & -\frac{1}{12} & 0 & 0 & 0 & 0 & 0 & 0 & 0 \\
\frac{1}{19} & -\frac{11}{2394} & -\frac{1}{63} & 0 & 0 & 0 & 0 & \frac{1}{10} & -\frac{1}{10} & -\frac{1}{36} & \frac{1}{36} & -\frac{1}{12} & \frac{1}{12} & 0 & 0 & 0 & 0 & 0 & 0 & 0 \\
\frac{1}{19} & -\frac{11}{2394} & -\frac{1}{63} & 0 & 0 & 0 & 0 & -\frac{1}{10} & \frac{1}{10} & -\frac{1}{36} & \frac{1}{36} & -\frac{1}{12} & \frac{1}{12} & 0 & 0 & 0 & 0 & 0 & 0 & 0 \\
\frac{1}{19} & \frac{4}{1197} & \frac{1}{252} & \frac{1}{10} & \frac{1}{40} & \frac{1}{10} & \frac{1}{40} & 0 & 0 & \frac{1}{36} & \frac{1}{72} & \frac{1}{12} & \frac{1}{24} & \frac{1}{4} & 0 & 0 & \frac{1}{8} & -\frac{1}{8} & 0 & \\
\frac{1}{19} & \frac{4}{1197} & \frac{1}{252} & -\frac{1}{10} & -\frac{1}{40} & \frac{1}{10} & \frac{1}{40} & 0 & 0 & \frac{1}{36} & \frac{1}{72} & \frac{1}{12} & \frac{1}{24} & -\frac{1}{4} & 0 & 0 & -\frac{1}{8} & -\frac{1}{8} & 0 & \\
\frac{1}{19} & \frac{4}{1197} & \frac{1}{252} & \frac{1}{10} & \frac{1}{40} & -\frac{1}{10} & -\frac{1}{40} & 0 & 0 & \frac{1}{36} & \frac{1}{72} & \frac{1}{12} & \frac{1}{24} & -\frac{1}{4} & 0 & 0 & \frac{1}{8} & \frac{1}{8} & 0 & \\
\frac{1}{19} & \frac{4}{1197} & \frac{1}{252} & -\frac{1}{10} & -\frac{1}{40} & -\frac{1}{10} & -\frac{1}{40} & 0 & 0 & \frac{1}{36} & \frac{1}{72} & \frac{1}{12} & \frac{1}{24} & \frac{1}{4} & 0 & 0 & -\frac{1}{8} & \frac{1}{8} & 0 & \\
\frac{1}{19} & \frac{4}{1197} & \frac{1}{252} & \frac{1}{10} & \frac{1}{40} & 0 & 0 & \frac{1}{10} & \frac{1}{40} & \frac{1}{36} & \frac{1}{72} & -\frac{1}{12} & -\frac{1}{24} & 0 & 0 & \frac{1}{4} & -\frac{1}{8} & 0 & \frac{1}{8} & \\
\frac{1}{19} & \frac{4}{1197} & \frac{1}{252} & -\frac{1}{10} & -\frac{1}{40} & 0 & 0 & \frac{1}{10} & \frac{1}{40} & \frac{1}{36} & \frac{1}{72} & -\frac{1}{12} & -\frac{1}{24} & 0 & 0 & -\frac{1}{4} & \frac{1}{8} & 0 & \frac{1}{8} & \\
\frac{1}{19} & \frac{4}{1197} & \frac{1}{252} & \frac{1}{10} & \frac{1}{40} & 0 & 0 & -\frac{1}{10} & -\frac{1}{40} & \frac{1}{36} & \frac{1}{72} & -\frac{1}{12} & -\frac{1}{24} & 0 & 0 & -\frac{1}{4} & -\frac{1}{8} & 0 & -\frac{1}{8} & \\
\frac{1}{19} & \frac{4}{1197} & \frac{1}{252} & -\frac{1}{10} & -\frac{1}{40} & 0 & 0 & -\frac{1}{10} & -\frac{1}{40} & \frac{1}{36} & \frac{1}{72} & -\frac{1}{12} & -\frac{1}{24} & 0 & 0 & \frac{1}{4} & \frac{1}{8} & 0 & -\frac{1}{8} & \\
\frac{1}{19} & \frac{4}{1197} & \frac{1}{252} & 0 & 0 & \frac{1}{10} & \frac{1}{40} & \frac{1}{10} & \frac{1}{40} & -\frac{1}{18} & -\frac{1}{36} & 0 & 0 & 0 & \frac{1}{4} & 0 & 0 & \frac{1}{8} & -\frac{1}{8} & \\
\frac{1}{19} & \frac{4}{1197} & \frac{1}{252} & 0 & 0 & -\frac{1}{10} & -\frac{1}{40} & \frac{1}{10} & \frac{1}{40} & -\frac{1}{18} & -\frac{1}{36} & 0 & 0 & 0 & -\frac{1}{4} & 0 & 0 & -\frac{1}{8} & -\frac{1}{8} & \\
\frac{1}{19} & \frac{4}{1197} & \frac{1}{252} & 0 & 0 & \frac{1}{10} & \frac{1}{40} & -\frac{1}{10} & -\frac{1}{40} & -\frac{1}{18} & -\frac{1}{36} & 0 & 0 & 0 & -\frac{1}{4} & 0 & 0 & \frac{1}{8} & \frac{1}{8} & \\
\frac{1}{19} & \frac{4}{1197} & \frac{1}{252} & 0 & 0 & -\frac{1}{10} & -\frac{1}{40} & -\frac{1}{10} & -\frac{1}{40} & -\frac{1}{18} & -\frac{1}{36} & 0 & 0 & 0 & \frac{1}{4} & 0 & 0 & -\frac{1}{8} & \frac{1}{8} &
\end{bmatrix}$$

The components of equilibrium moments are given as (Premnath *et al.* 2009a):

$$m_0^{eq} = \rho^{eq} = \rho, \qquad m_1^{eq} = e^{eq} = \rho(-11 + 19(u^2 + v^2 + w^2)),$$

$$m_2^{eq} = \epsilon^{eq} = \rho(3 - \tfrac{11}{2}(u^2 + v^2 + w^2)), \quad m_3^{eq} = j_x^{eq} = j_x, \qquad m_4^{eq} = q_x^{eq} = -\tfrac{2}{3}j_x,$$

$$m_5^{eq} = j_y^{eq} = j_y, \qquad m_6^{eq} = q_y^{eq} = -\tfrac{2}{3}j_y, \; m_7^{eq} = j_z^{eq} = j_z, \qquad m_8^{eq} = q_z^{eq} = -\tfrac{2}{3}j_z,$$

$$m_9^{eq} = 3p_{xx}^{eq} = \tfrac{3{j_x}^2 - \vec{j}\times\vec{j}}{\rho}, \qquad m_{10}^{eq} = 3\pi_{xx}^{eq} = -\tfrac{3}{2}p_{xx}^{eq}, \qquad m_{11}^{eq} = p_{ww}^{eq} = \rho(v^2 - w^2),$$

$$m_{12}^{eq} = \pi_{ww}^{eq} = -\tfrac{1}{2}p_{ww}^{eq}, \qquad m_{13}^{eq} = p_{xy}^{eq} = \rho uv, \quad m_{14}^{eq} = p_{yz}^{eq} = \rho vw, \quad m_{15}^{eq} = p_{xz}^{eq} = \rho uw,$$

$$m_{16}^{eq} = m_x^{eq} = 0, \qquad m_{17}^{eq} = m_y^{eq} = 0, \qquad m_{18}^{eq} = m_z^{eq} = 0.$$

The components of source term in moment space are given as (Premnath *et al.* 2009a):

$$S_{S0} = 0, \qquad S_{S1} = 38\big(F_x u + F_y v + F_z w\big), \qquad S_{S2} = -11\big(F_x u + F_y v + F_z w\big),$$

$$S_{S3} = F_x, \qquad S_{S4} = -\tfrac{2}{3}F_x, \;\; S_{S5} = F_y, \qquad S_{S6} = -\tfrac{2}{3}F_y, \;\; S_{S7} = F_z, \qquad S_{S8} = -\tfrac{2}{3}F_z,$$

$$S_{S9} = 2\big(2F_x u - F_y v - F_z w\big), \qquad S_{S10} = -\big(2F_x u - F_y v - F_z w\big), \qquad S_{S11} = 2\big(F_y v - F_z w\big),$$

$$S_{S12} = -\big(F_y v - F_z w\big), \qquad S_{S13} = \big(F_x v + F_y u\big), \;\; S_{S14} = \big(F_y w + F_z v\big), \;\; S_{S15} = (F_x w + F_z u),$$

$$S_{S16} = 0, \qquad S_{S17} = 0, \qquad S_{S18} = 0.$$

The values of the diagonal collision matrix (Hossain *et al.* 2015):

$$s_1 = s_4 = s_6 = s_8 = 1.0, \qquad s_2 = 1.19, \qquad s_3 = s_{11} = s_{13} = 1.40,$$

$$s_5 = s_7 = s_9 = 1.20, \;\; s_{10} = \; s_{12} = \; s_{14} = \; s_{15} = \; s_{16} = 1.9857, \;\; S_{17} = S_{18} = S_{19} = 1.98.$$